

Cell surface and intracellular auxin signalling for H⁺ fluxes in root growth

Nature

Li, Lanxin; Verstraeten, Inge; Roosjen, Mark; Takahashi, Koji; Rodriguez, Lesia et al

<https://doi.org/10.1038/s41586-021-04037-6>

This publication is made publicly available in the institutional repository of Wageningen University and Research, under the terms of article 25fa of the Dutch Copyright Act, also known as the Amendment Taverne. This has been done with explicit consent by the author.

Article 25fa states that the author of a short scientific work funded either wholly or partially by Dutch public funds is entitled to make that work publicly available for no consideration following a reasonable period of time after the work was first published, provided that clear reference is made to the source of the first publication of the work.

This publication is distributed under The Association of Universities in the Netherlands (VSNU) 'Article 25fa implementation' project. In this project research outputs of researchers employed by Dutch Universities that comply with the legal requirements of Article 25fa of the Dutch Copyright Act are distributed online and free of cost or other barriers in institutional repositories. Research outputs are distributed six months after their first online publication in the original published version and with proper attribution to the source of the original publication.

You are permitted to download and use the publication for personal purposes. All rights remain with the author(s) and / or copyright owner(s) of this work. Any use of the publication or parts of it other than authorised under article 25fa of the Dutch Copyright act is prohibited. Wageningen University & Research and the author(s) of this publication shall not be held responsible or liable for any damages resulting from your (re)use of this publication.

For questions regarding the public availability of this publication please contact openscience.library@wur.nl

Cell surface and intracellular auxin signalling for H⁺ fluxes in root growth

<https://doi.org/10.1038/s41586-021-04037-6>

Received: 4 February 2021

Accepted: 17 September 2021

Published online: 27 October 2021



Lanxin Li^{1,12}, Inge Verstraeten^{1,12}, Mark Roosen², Koji Takahashi^{3,4}, Lesia Rodriguez¹, Jack Merrin¹, Jian Chen^{5,6}, Lana Shabala⁷, Wouter Smet^{5,6}, Hong Ren⁸, Steffen Vanneste^{5,9,10}, Sergey Shabala^{7,11}, Bert De Rybel^{5,6}, Dolf Weijers², Toshinori Kinoshita^{3,4}, William M. Gray⁸ & Jiri Friml^{1✉}

Growth regulation tailors development in plants to their environment. A prominent example of this is the response to gravity, in which shoots bend up and roots bend down¹. This paradox is based on opposite effects of the phytohormone auxin, which promotes cell expansion in shoots while inhibiting it in roots via a yet unknown cellular mechanism². Here, by combining microfluidics, live imaging, genetic engineering and phosphoproteomics in *Arabidopsis thaliana*, we advance understanding of how auxin inhibits root growth. We show that auxin activates two distinct, antagonistically acting signalling pathways that converge on rapid regulation of apoplastic pH, a causative determinant of growth. Cell surface-based TRANSMEMBRANE KINASE1 (TMK1) interacts with and mediates phosphorylation and activation of plasma membrane H⁺-ATPases for apoplast acidification, while intracellular canonical auxin signalling promotes net cellular H⁺ influx, causing apoplast alkalization. Simultaneous activation of these two counteracting mechanisms poises roots for rapid, fine-tuned growth modulation in navigating complex soil environments.

Auxin, a major growth regulator in plants, acts oppositely in shoots and roots. In shoots, canonical/intracellular auxin TRANSPORT INHIBITOR RESPONSE1 and AUXIN-SIGNALING F-BOX (TIR1/AFB) receptors activate H⁺ pumps by downstream transcriptional regulation to acidify the apoplast and promote cell elongation^{3,4}, in accordance with the acid growth theory, which postulates that low apoplastic pH promotes growth⁵. In roots of many species, including *Arabidopsis*, auxin inhibits growth. These contrasting responses are the basis for positive versus negative bending of roots and shoots in response to gravity and light¹. The inhibitory effect of auxin in roots also involves TIR1/AFB receptors, but the rapid timing of inhibition points towards an unknown non-transcriptional signalling branch⁶. A cell surface-based pathway involving TMK1 regulates development⁷, including differential growth in the apical hook⁸, although the role of this pathway in auxin-regulated root growth remains unclear. Hence, the auxin signalling mechanism and the downstream processes for regulating root growth have remained unclear.

In this study, we show that antagonistic actions of intracellular TIR1/AFB and cell surface TMK1 auxin signalling converge on regulation of apoplastic pH, which we confirm as the key cellular mechanism that allows immediate and sensitive regulation of root growth.

Growth inhibition correlates with H⁺ influx

Auxin rapidly inhibits root growth through a non-transcriptional branch of TIR1/AFB signalling⁶. Although several cellular processes, including

cortical microtubule (CMT) re-orientation^{9,10}, vacuolar fragmentation¹¹ and apoplastic pH changes^{12–14}, have been implicated in this process, its causal mechanism remains unidentified.

We critically re-evaluated the kinetics of these processes using vRootchip⁶ (Extended Data Fig. 1a) in combination with vertical confocal microscopy¹⁵. Growth inhibition following treatment with 10 nM of the naturally occurring auxin indole-3-acetic acid (IAA) was observed within 30 s (ref. ⁶). By contrast, less than 5% of CMTs in elongating epidermal cells had re-oriented after 1 min, even at 100 nM IAA, and pharmacological inhibition of this re-orientation had no effect on auxin-induced growth inhibition (Extended Data Fig. 1b–f). Similarly, we could not detect changes in vacuolar morphology in elongating cells even after 30 min of treatment with 100 nM IAA (Extended Data Fig. 1g). These results argue against direct involvement of CMT re-orientation and vacuole constriction in the rapid growth inhibition triggered by auxin.

To evaluate the kinetics of apoplastic pH, we applied a membrane-impermeable ratiometric pH indicator, 8-hydroxypyrene-1, 3,6-trisulfonic acid (HPTS), and imaged apoplastic pH while simultaneously tracking root tip growth. We detected an apoplastic pH gradient¹² in the root, with pH decreasing from the transition to the elongation zone; regardless of their position, all cells showed a rapid (30-s) increase in apoplastic pH following IAA treatment (Fig. 1a, b and Extended Data Fig. 2a). These experiments provide higher temporal and spatial resolution than previous observations of auxin-induced apoplast alkalization¹² and reveal that auxin-triggered alkalization and root growth

¹Institute of Science and Technology (IST) Austria, Klosterneuburg, Austria. ²Laboratory of Biochemistry, Department of Agrotechnology and Food Sciences, Wageningen University, Wageningen, the Netherlands. ³Institute of Transformative Bio-Molecules, Division of Biological Science, Nagoya University Chikusa, Nagoya, Japan. ⁴Graduate School of Science, Nagoya University Chikusa, Nagoya, Japan. ⁵Department of Plant Biotechnology and Bioinformatics, Ghent University, Ghent, Belgium. ⁶VIB Center for Plant Systems Biology, Ghent, Belgium. ⁷Tasmanian Institute of Agriculture, College of Science and Engineering, University of Tasmania, Hobart, Tasmania, Australia. ⁸Department of Plant & Microbial Biology, University of Minnesota, St. Paul, MN, USA. ⁹Laboratory of Plant Growth Analysis, Ghent University Global Campus, Incheon, Republic of Korea. ¹⁰Department of Plants and Crops, HortiCell, Ghent University, Ghent, Belgium. ¹¹International Research Centre for Environmental Membrane Biology, Foshan University, Foshan, China. ¹²These authors contributed equally: Lanxin Li and Inge Verstraeten. ✉e-mail: jiri.friml@ist.ac.at

inhibition occur simultaneously (Fig. 1b). The pH increase was robust and extended to the external medium (Extended Data Fig. 2b). Using the *PM-Cyto* reporter for monitoring intracellular pH¹⁶, we also detected a simultaneous (30-s) decrease in plasma membrane (PM)-adjacent cytosolic pH after treatment with 5 nM IAA (Fig. 1c). Concomitant apoplastic pH increase and intracellular pH decrease implies H⁺ influx into cells. This was confirmed using non-invasive microelectrodes monitoring direct net H⁺ exchange across the PM of elongating root epidermal cells after IAA treatment (Extended Data Fig. 2c), consistent with similar observations in root hair cells¹⁷.

Overall, auxin triggers rapid apoplast alkalization by increasing net cellular H⁺ influx. Spatial and temporal correlation of this process with root growth inhibition suggests apoplast alkalization as the underlying cellular mechanism for inhibition.

Apoplastic pH regulates root growth

To investigate the causal relationship between apoplast alkalization and root growth inhibition, we manipulated apoplastic pH by changing the pH of the medium (Extended Data Fig. 2d, e) and monitoring the impact on root growth. This extended previous observations from prolonged (2.5-h) external extreme pH manipulation¹². Replacement of the basal medium (pH 5.8) with more alkaline (pH 6.15) medium caused an instant reduction in root growth; the growth rate was rapidly restored after washout with medium at the original pH (Fig. 1d, e). Gradual alkalization of the medium resulted in gradual root growth inhibition (Extended Data Fig. 2f). Replacing the basal medium with more acidic (pH 5.1) medium instantly increased root growth, while washout restored the original growth rate (Fig. 1f, g).

Thus, exogenous manipulation of apoplastic pH has immediate and reversible effects on root growth, with alkaline pH inhibiting and acidic pH promoting growth. This strongly supports the idea that auxin-induced apoplast alkalization is the key downstream cellular mechanism for rapid root growth inhibition.

Auxin triggers activation of PM H⁺-ATPases

Apoplast alkalization in response to auxin occurs too quickly to involve transcriptional regulation, as also confirmed by pharmacological interference with translation (cycloheximide) or transcription (cordycepin) (Extended Data Fig. 3a, b). To gain insights into the underlying mechanism, we mined recent datasets from mass spectrometry (MS)-aided phosphoproteomics in wild-type (WT) root tips treated for 2 min with 100 nM IAA¹⁸. Among the differentially phosphorylated targets were two PM H⁺-ATPases, AHA1 and AHA2. Multiple putative auxin-regulated phosphorylation sites were identified in the autoinhibitory C-terminal regions of these proteins, with phosphorylation leading to both activation and deactivation of their H⁺-pump activity¹⁹ (Fig. 2a and Supplementary Table 1).

To test whether auxin changes the activity of PM H⁺-ATPases in roots, we performed an ATP hydrolysis assay measuring the hydrolytic release of inorganic phosphate from ATP, representing the activity of PM H⁺-ATPases. After 1 h of treatment with 100 nM IAA, we detected increased ATP hydrolysis activity in root protein extracts (Fig. 2b). This suggests that auxin activates H⁺ pumps, which should, however, lead to apoplast acidification instead of the observed alkalization (Fig. 1b).

We next reanalysed the phosphoproteomics data specifically for phosphorylation of Thr947 in AHA2, a well-known activation site¹⁹. Thr947 was significantly more phosphorylated after IAA treatment (Fig. 2c). To confirm this, we used an antibody against the AHA2 catalytic domain and an antibody against phosphorylated Thr947, revealing that 10 nM IAA induced phosphorylation of Thr947 in 10 min (Extended Data Fig. 3c). Thus, auxin induces AHA2 phosphorylation, leading to its activation.

Our results show that auxin rapidly induces AHA phosphorylation, leading to H⁺-pump activation in roots. This is similar to what occurs in

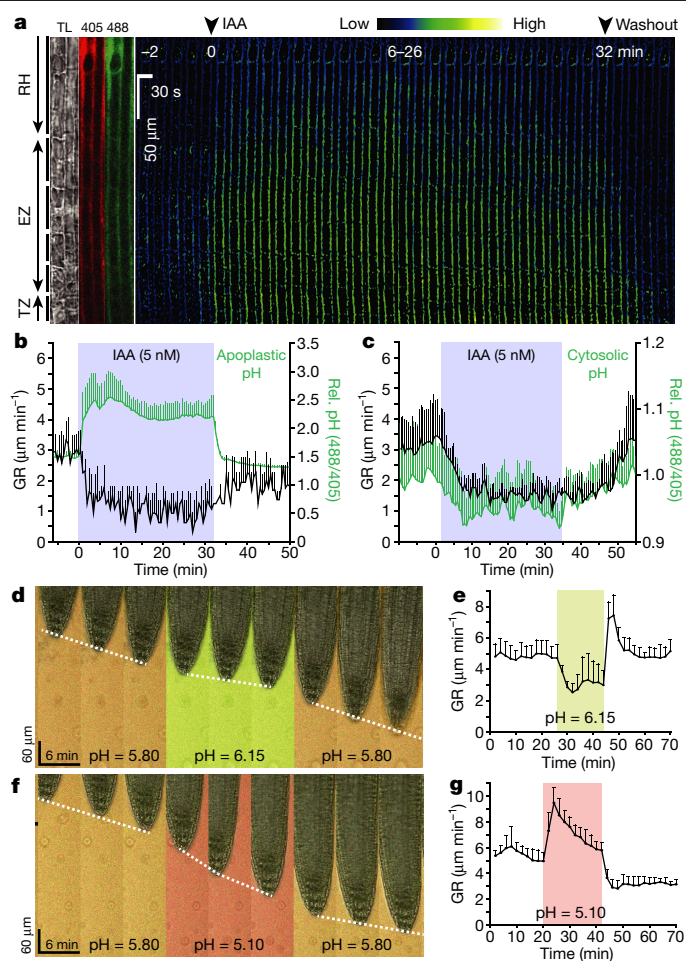


Fig. 1 | Auxin rapidly inhibits root growth by apoplast alkalization.

a, Time-lapse imaging of apoplastic pH in root tip epidermal cells treated with 5 nM IAA followed by washout in vRootchip. Ratiometric (488 nm/405 nm) imaging of HPST staining was used to monitor pH in root hair (RH), the elongation zone (EZ) and the transition zone (TZ). TL, transmitted light. **b**, Quantification of apoplastic pH and growth rate (GR) in the elongation zone following treatment with 5 nM IAA and washout as in **a**. Data are shown as the mean of four roots + s.d. **c**, Quantification of cytosolic pH (using the *PM-Cyto* reporter) and growth rate in the elongation zone following treatment with 5 nM IAA in vRootchip. Data are shown as the mean of three roots + s.d. **d–g**, Root growth response to alkaline (pH 6.15) (**d**) or acidic (pH 5.10) (**f**) medium. The dashed white lines track the root tip over time. Quantifications of growth rate in **d** ($n = 8$ roots) and **f** ($n = 7$ roots) are shown in **e** and **g**, respectively. Shaded areas represent the duration of treatment. Data are shown as the mean + s.d.

shoots^{20,21}, but opposite to the observed auxin-induced H⁺ influx (Fig. 1), suggesting that in roots H⁺-pump activation may act antagonistically to auxin-triggered apoplast alkalization.

H⁺-ATPases counteract apoplast alkalization

To better understand the role of H⁺-pump activation during auxin-triggered apoplast alkalization, we used the fungal toxin fusaric acid (FA), which stabilizes pumps in the activated form¹⁹ without affecting transcriptional signalling by auxin (Extended Data Fig. 3d). FA caused rapid apoplast acidification and promoted root growth¹² (Extended Data Fig. 3e, f), opposite to auxin. When FA and IAA were applied simultaneously or sequentially, we observed an intermediate response proportional to the auxin/FA ratio (Fig. 2d and Extended Data Fig. 3e–k). These results suggest that FA-triggered H⁺-ATPase activation and IAA-triggered apoplast alkalization act antagonistically.

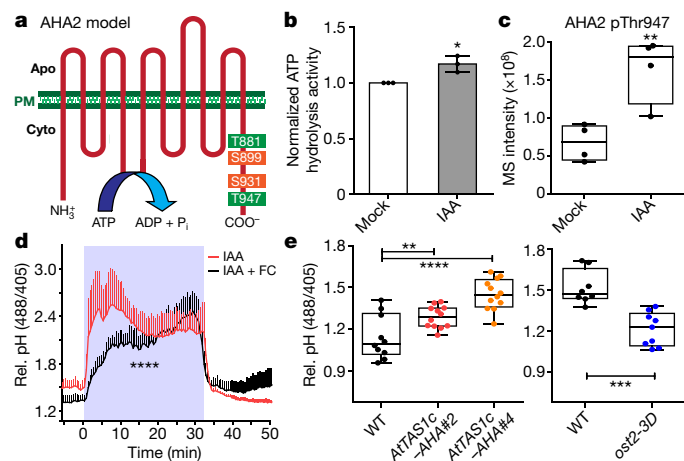


Fig. 2 | Auxin-triggered H^+ -ATPase activation counteracts auxin-triggered apoplast alkalization. **a**, AHA2 phosphosites identified in phosphoproteomic analysis of roots after 2 min of treatment with 100 nM IAA. Green, activation of H^+ translocation; orange, inhibition of H^+ translocation. **b**, Quantification of ATP hydrolysis in roots treated for 1 h with 100 nM IAA normalized to roots with mock treatment. Bars indicate the mean of three biological replicates \pm s.d. Unpaired t -test, $^*P = 0.0138$. **c**, Phosphorylation at Thr947 of AHA2 in roots after 2 min of treatment with 100 nM IAA. $n = 4$ biological replicates. Box plots depict the minimum to maximum and mean \pm s.d. Unpaired t -test, $^{**}P = 0.0077$. **d**, Activation of H^+ -ATPases by 10 μ M FC affects alkalization induced by 10 nM IAA. The shaded area represents the duration of treatment. Data are shown as the mean of four roots \pm s.d. $^{****}P \leq 0.0001$ from 0–32 min, two-way ANOVA. **e**, Apoplast alkalization in *AtTAS1c-AHA#2* and *AtTAS1c-AHA#4* roots with decreased *AHA* transcripts ($n > 9$ roots) and *oost2-3D* roots with *AHA1* gain of function ($n > 5$ roots) after 30 min of treatment with 5 nM IAA normalized to roots with mock treatment. Box plots depict the minimum to maximum and mean \pm s.d. $^{**}P \leq 0.01$, $^{***}P \leq 0.001$, $^{****}P \leq 0.0001$, one-way ANOVA.

To test this genetically, we analysed the auxin response of loss- and gain-of-function *aha* mutants. Roots with *AHA1* and *AHA2* mutated individually showed no growth defects (Extended Data Fig. 3l), while the double mutant is embryonic lethal¹⁹. To overcome the redundancy, we used a synthetic *trans*-acting small interfering RNA (siRNA) targeting *AHA1*, *AHA2*, *AHA7* and *AHA11* (*AtTAS1c-AHA*), expressed from the *PIN2* promoter²². *AHA* transcripts were downregulated in two independent transgenic lines (Extended Data Fig. 3m), which were both hypersensitive to auxin for apoplast alkalization (Fig. 2e) and root growth inhibition (Extended Data Fig. 3n). In contrast, constitutive activation of *AHA1* in the *ost2-3D* mutant resulted in decreased sensitivity to auxin in apoplastic pH (Fig. 2e) and root growth (Extended Data Fig. 3n).

These observations show that H^+ -ATPase activation antagonizes auxin-induced apoplast alkalization in roots.

TMK1 interacts with H^+ -ATPases

To address how auxin signalling regulates apoplastic pH, we performed co-immunoprecipitation (co-IP) followed by MS-assisted identification of proteins associated with either the TIR1 or AFB1 receptor or the PM-localized TMK1 auxin signalling component⁷ (Extended Data Fig. 4a). For the TIR1/AFB1 receptors, this approach did not reveal any relevant components, while for TMK1 the AHA H^+ -ATPases were among the top most enriched associated peptides (Extended Data Fig. 4b–d and Supplementary Table 2 and 3).

We verified the interaction between AHA proteins and TMK1 by co-IP from *pTMK1::TMK1-FLAG* (Fig. 3a) and *pAHA2::AHA2-GFP* (Extended Data Fig. 4e) roots. From TMK1-FLAG pulldowns, we detected associated

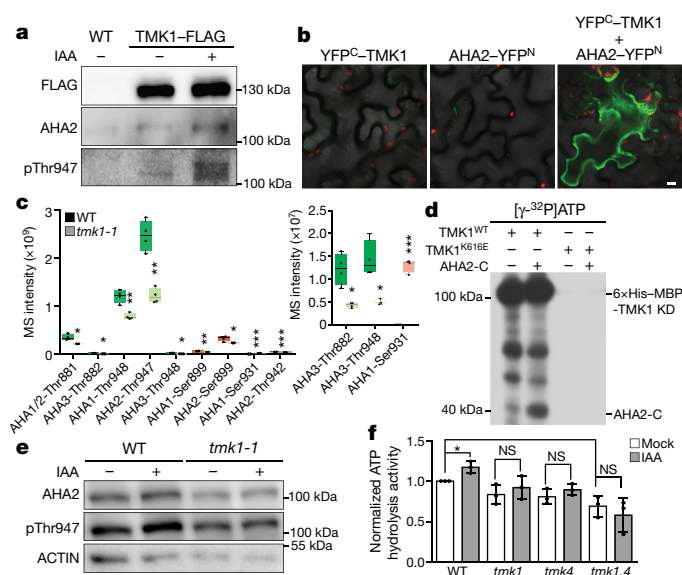


Fig. 3 | TMK1 directly mediates auxin-induced H^+ -ATPase activation.

a, Co-IP from *pTMK1::TMK1-FLAG* roots after 30 min of treatment with 100 nM IAA, followed by western blot detection of AHA2 and AHA2 phosphorylated at Thr947. **b**, BiFC in *Nicotiana benthamiana* leaves transiently transformed with constructs encoding YFP^C-TMK1 and AHA2-YFP^N, alone and in combination. Scale bar, 10 μ m. **c**, Phosphorylation of AHA phosphosites in the *tmk1-1* and WT lines (box plot outlines as indicated in the key). Green, known activation function; orange, known inhibitory function; grey, unknown function. The inset shows sites with lower detected values. $n = 4$ biological replicates. Box plots depict the minimum to maximum and mean \pm s.d. Student's t -test, $^*P \leq 0.05$, $^{**}P \leq 0.01$, $^{***}P \leq 0.001$. **d**, In vitro kinase assay with [γ -³²P]ATP. C-terminal AHA2 (AHA2-C) and the kinase domain (KD) of TMK1^{WT} or kinase-dead TMK1^{K616E}. AHA2-C is phosphorylated by TMK1^{WT} but not by TMK1^{K616E}. Autophosphorylation of TMK1^{WT} is also detected. **e**, Western blot analysis of phosphorylation at AHA2 Thr947 in WT and *tmk1-1* roots treated for 1 h with 100 nM IAA. **f**, Auxin-induced ATP hydrolysis activity is impaired in *tmk* mutants (1 h of treatment with 100 nM IAA). Levels were normalized to those in mock-treated WT roots. Data are shown as the mean of three biological replicates \pm s.d. $^*P \leq 0.05$, one-way ANOVA; NS, not significant ($P > 0.05$).

AHA2, and reciprocally, from AHA2-GFP pulldowns, we detected TMK1. Additional in vivo verification was provided by bimolecular fluorescence complementation (BiFC) in tobacco leaves co-transformed with constructs for TMK1 and AHA2 (Fig. 3b and Extended Data Fig. 4f, g).

These observations show that TMK1, the component of cell surface auxin signalling, interacts with PM H^+ -ATPase.

TMK1 mediates the effect of auxin on H^+ -ATPases

To test the role of TMK1 in H^+ -ATPase phosphorylation, we performed phosphoproteomic analysis in roots from *tmk1-1* plants (which have a T-DNA insertion in *TMK1*) compared with WT roots and detected strong hypophosphorylation of AHAs (Fig. 3c and Supplementary Table 1), suggesting TMK1 involvement in H^+ -ATPase phosphorylation.

To verify this, we cloned *p35S::TMK1-HA* and two versions encoding kinase-dead mutants with mutations mapping to the ATP-binding site, TMK1^{K616E} and TMK1^{K616R}. Transient overexpression of the WT construct (TMK1^{WT}), but not the kinase-dead constructs, resulted in rapid wilting of tobacco leaves (Extended Data Fig. 5a), an effect consistent with PM H^+ -ATPase activation²³. We further generated *Arabidopsis* dexamethasone (DEX)-inducible gain-of-function lines. Compared with TMK1^{WT} root extracts, those from TMK1^{K616R} seedlings did not show IAA-induced phosphorylation of Thr947 in the AHA H^+ -ATPases (Extended Data Fig. 5b). Importantly, in vitro [γ -³²P]ATP kinase assays confirmed that TMK1^{WT}, but not kinase-dead TMK1^{K616E},

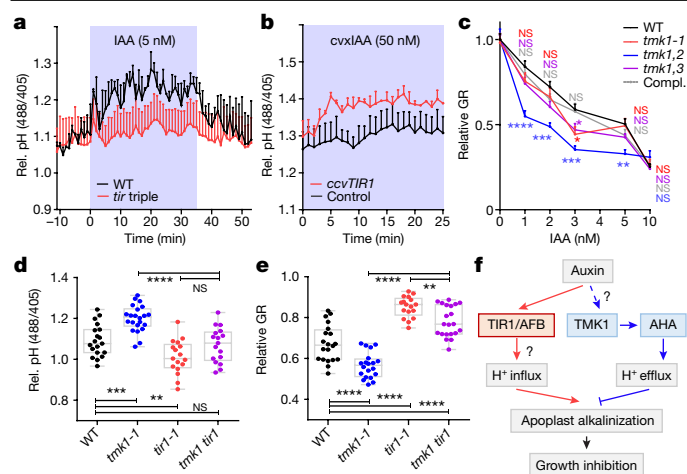


Fig. 4 | Antagonistic TIR1/AFB and TMK1 signalling converge on apoplastic pH for growth regulation. **a**, Apoplastic pH response in *tir* triple mutant (red) compared with WT (black) roots in vRootchip. Data are shown as the mean of three (*tir* triple) and two (WT) roots + s.e.m. **b**, Apoplastic pH analysis in *ccvTIR1* (red) compared with control (black) roots in response to *cvxIAA* in vRootchip. Data are shown as the mean of two (*ccvTIR1*) and three (control) roots + s.e.m. The shaded areas in **a** and **b** represent the duration of treatment. **c**, Dose–response curves for root growth inhibition in *tmk1*-related mutants and *pTMK1::TMK1-FLAG* in *tmk1-1* (compl.). Relative growth rate is the ratio of the growth rates with auxin and mock treatment in the same genotype. $n > 15$ roots. * $P \leq 0.05$, ** $P \leq 0.01$, *** $P \leq 0.001$, **** $P \leq 0.0001$, Welch ANOVA; NS, not significant ($P > 0.05$). **d, e**, Apoplastic pH (**d**) and root growth (**e**) in *tmk1-1*, *tir1-1* and *tmk1 tir1* mutants in response to treatment with 5 nM IAA for 50 min (**d**) and 6 h (**e**). $n > 16$ roots. Box plots depict the minimum to maximum and mean \pm s.d. ** $P \leq 0.01$, *** $P \leq 0.001$, **** $P \leq 0.0001$, one-way ANOVA; NS, not significant ($P > 0.05$). **f**, Model for auxin-induced root growth regulation. An intracellular, non-transcriptional branch of the TIR1/AFB signalling pathway (red) mediates rapid H^+ influx for apoplast alkalization and growth inhibition. Cell surface TMK1 activates H^+ pumps (AHAs; blue) to acidify the apoplast and promote growth.

directly phosphorylates the AHA2 C-terminal domain (Fig. 3d and Extended Data Fig. 5c).

Next, we analysed different *tmk* loss-of-function mutants. We detected less auxin-induced AHA2 phosphorylation in *tmk1-1* roots, as well as in roots from the *tmk1,3* and stunted *tmk1,4* double mutants (Fig. 3e and Extended Data Fig. 5d, e). In addition, the ATP hydrolysis assay showed that auxin-stimulated H^+ -ATPase activity was diminished in *tmk1-1*, *tmk1,4* and *tmk1,4* roots (Fig. 3f).

Collectively, these findings demonstrate that active TMK1 mediates auxin-triggered phosphorylation and activation of H^+ -ATPases in roots.

TIR1 and TMK1 converge on pH regulation

Our results show that TMK1 directly phosphorylates and activates PM H^+ -ATPases, leading to apoplast acidification (Figs. 2 and 3). This is opposite to the observed auxin-induced apoplast alkalization leading to growth inhibition (Fig. 1), which prompted us to address the underlying signalling mechanism.

aux1-100 mutants with mutations in the auxin influx transporter *AUXIN RESISTANT1* (*AUX1*) that are impaired in uptake of IAA²⁴ were less sensitive to auxin, in terms of both growth inhibition⁶ (Extended Data Fig. 6b, d) and apoplast alkalization (Extended Data Fig. 6a, c), suggesting a requirement for intracellular auxin perception.

Given that intracellular TIR1/AFB receptors mediate auxin-triggered rapid growth inhibition⁶, we evaluated apoplastic pH in parallel to growth in the *tir1 afb2 afb3* (*tir* triple) mutant. *tir* triple roots were resistant to IAA with respect to both apoplast alkalization and growth inhibition (Fig. 4a and Extended Data Fig. 6e). AFB1 with its

predominantly cytosolic localization has been proposed to be the major auxin receptor mediating the rapid effects of auxin in growth and membrane depolarization^{25,26}. We found that both TIR1 and AFB1 contribute to this regulation: while the *tir1-10* mutant was more resistant to auxin in the long term, the *afb1-3* mutant showed pronounced resistance to rapid auxin-induced effects (Extended Data Fig. 6h–k). We also applied the auxin antagonist PEO-IAA to block downstream TIR1/AFB signalling²⁷. Simultaneous addition of 10 μ M PEO-IAA and 5 nM IAA prevented apoplast alkalization and growth inhibition (Extended Data Fig. 6f, g). We also took advantage of the *cvxIAA*–*ccvTIR1* system, in which the engineered concave (*ccv*) TIR1 receptor cannot interact with naturally occurring IAA and only interacts with a synthetic convex (*cvx*) IAA, allowing specific activation of TIR1 signalling²⁸. Application of 50 nM *cvxIAA* resulted in apoplastic alkalization in *ccvTIR1* roots (Fig. 4b), confirming that specific activation of TIR1 is sufficient to trigger apoplast alkalization. These approaches demonstrate involvement of intracellular TIR1/AFB receptors in auxin-induced apoplast alkalization.

This effect is counteracted by cell surface TMK1-mediated H^+ -ATPase activation for apoplast acidification and growth promotion. Indeed, in the steady state, TMK1 is redundantly required for root growth, as demonstrated by shorter roots in *tmk* mutants⁷ (Extended Data Fig. 6l). In response to low concentrations of auxin, *tmk1*-related mutants were hypersensitive (Fig. 4c), while overexpressing TMK1 (*pUBQ10::TMK1-3HA*) led to slight auxin resistance (Extended Data Fig. 6m). This resembles the findings with the corresponding loss- and gain-of-function *aha* mutants (Fig. 2), providing additional support for the antagonistic, growth-promoting role of TMK-mediated AHA activity.

We also created a *tmk1 tir1* double mutant and analysed the effect of auxin on apoplastic pH and root growth. As expected, *tmk1 tir1* mutants showed intermediate auxin sensitivity when compared with the single mutants, in terms of both growth and apoplastic pH (Fig. 4d, e and Extended Data Fig. 6n, o).

Collectively, we propose that auxin inactivates two antagonistic signalling pathways: (1) cell surface TMK1-mediated H^+ export acidifying the apoplast and (2) more dominant intracellular TIR1/AFB-dependent apoplast alkalization leading to rapid growth inhibition (Fig. 4f).

Conclusions

Our findings provide novel insights into the long-standing question of how plant root growth is regulated. In particular, we address the old mystery of opposite growth regulation in shoots and roots by the phytohormone auxin, and we also clarify the downstream cellular mechanism of auxin-triggered root growth inhibition.

Auxin regulates root growth very rapidly, using a non-transcriptional branch of a signalling pathway downstream of the intracellular TIR1/AFB receptors⁶. The same branch mediates apoplast alkalization, which we confirm as the causative cellular mechanism for root growth regulation, thus extending the classical acid growth theory to root growth inhibition.

Remarkably, auxin-induced apoplast alkalization in roots does not occur through regulation of PM H^+ -ATPases as observed in shoots, where TIR1/AFB transcriptional auxin signalling leads to PM H^+ -ATPase activation and apoplast acidification^{4,20}. Instead, in roots, PM H^+ -ATPases are phosphorylated and activated by cell surface TMK1-based auxin signalling, which leads to apoplast acidification. This mechanism acts antagonistically to the more dominant TIR1/AFB-mediated alkalization.

A key open question concerns the downstream mechanism by which TIR1/AFB signalling mediates apoplast alkalization. A plausible scenario would be a rapid increase in H^+ permeability across the PM, which is intertwined with changes in PM potential²⁵ (Extended Data Fig. 7a–c). Such auxin-triggered H^+ influx cannot be easily explained by IAA[−]/2H⁺ symport via the AUX1 influx carrier as proposed¹⁷ (Extended Data Fig. 7d) and does not seem to require the PM-localized receptor-like

kinase FERONIA, a mediator of rapid apoplast alkalization in response to RAPID ALKALINIZATION FACTOR 1 (RALF1)²⁹, as evidenced by normal auxin-induced rapid root growth inhibition in the mutant (Extended Data Fig. 8). On the other hand, this influx may involve previously reported¹⁴ auxin-triggered cytosolic Ca²⁺ transients (Extended Data Fig. 9). Another persistent mystery is the auxin perception mechanism for the TMK1 pathway. Does this occur via direct activation of TMK1 by auxin or through another yet to be established auxin receptor?

With cell surface-based TMK1 activating H⁺ pumps and intracellular TIR1/AFB signalling causing net cellular H⁺ influx, two auxin-triggered mechanisms converge on regulation of extracellular pH, which directly determines root growth. This seemingly counterproductive simultaneous ‘gas and brake’ action presumably poises the root tip for rapid and flexible directional growth changes during the challenging task of navigating complex soil environments.

Online content

Any methods, additional references, Nature Research reporting summaries, source data, extended data, supplementary information, acknowledgements, peer review information; details of author contributions and competing interests; and statements of data and code availability are available at <https://doi.org/10.1038/s41586-021-04037-6>.

1. Estelle, M. Plant tropisms: the ins and outs of auxin. *Curr. Biol.* **6**, 1589–1591 (1996).
2. Gallei, M., Luschig, C. & Friml, J. Auxin signalling in growth: Schrödinger’s cat out of the bag. *Curr. Opin. Plant Biol.* **53**, 43–49 (2020).
3. Spartz, A. K. et al. SAUR inhibition of PP2C-D phosphatases activates plasma membrane H⁺-ATPases to promote cell expansion in *Arabidopsis*. *Plant Cell* **26**, 2129–2142 (2014).
4. Fendrych, M., Leung, J. & Friml, J. TIR1/AFB–Aux/IAA auxin perception mediates rapid cell wall acidification and growth of *Arabidopsis* hypocotyls. *eLife* **5**, e19048 (2016).
5. Du, M., Spalding, E. P. & Gray, W. M. Rapid auxin-mediated cell expansion. *Annu. Rev. Plant Biol.* **71**, 379–402 (2020).
6. Fendrych, M. et al. Rapid and reversible root growth inhibition by TIR1 auxin signalling. *Nat. Plants* **4**, 453–459 (2018).
7. Dai, N., Wang, W., Patterson, S. E. & Bleeker, A. B. The TMK subfamily of receptor-like kinases in *Arabidopsis* display an essential role in growth and a reduced sensitivity to auxin. *PLoS ONE* **8**, e60990 (2013).
8. Cao, M. et al. TMK1-mediated auxin signalling regulates differential growth of the apical hook. *Nature* **568**, 240–243 (2019).
9. Chen, X. et al. Inhibition of cell expansion by rapid ABP1-mediated auxin effect on microtubules. *Nature* **516**, 90–93 (2014).

10. Adamowski, M., Li, L. & Friml, J. Reorientation of cortical microtubule arrays in the hypocotyl of *Arabidopsis thaliana* is induced by the cell growth process and independent of auxin signaling. *Int. J. Mol. Sci.* **20**, 3337 (2019).
11. Scheuring, D. et al. Actin-dependent vacuolar occupancy of the cell determines auxin-induced growth repression. *Proc. Natl Acad. Sci. USA* **113**, 452–457 (2016).
12. Barbez, E., Dünser, K., Gaidora, A., Lendl, T. & Busch, W. Auxin steers root cell expansion via apoplastic pH regulation in *Arabidopsis thaliana*. *Proc. Natl Acad. Sci. USA* **114**, E4884–E4893 (2017).
13. Monshausen, G. B., Miller, N. D., Murphy, A. S. & Gilroy, S. Dynamics of auxin-dependent Ca²⁺ and pH signaling in root growth revealed by integrating high-resolution imaging with automated computer vision-based analysis. *Plant J.* **65**, 309–318 (2011).
14. Shih, H.-W., DePew, C. L., Miller, N. D. & Monshausen, G. B. The cyclic nucleotide-gated channel CNGC14 regulates root gravitropism in *Arabidopsis thaliana*. *Curr. Biol.* **25**, 3119–3125 (2015).
15. Von Wangenheim, D. et al. Live tracking of moving samples in confocal microscopy for vertically grown roots. *eLife* **6**, e26792 (2017).
16. Martinière, A. et al. Uncovering pH at both sides of the root plasma membrane interface using noninvasive imaging. *Proc. Natl Acad. Sci. USA* **115**, 6488–6493 (2018).
17. Dindas, J. et al. AUX1-mediated root hair auxin influx governs SCF^{TIR1/AFB}-type Ca²⁺ signaling. *Nat. Commun.* **9**, 1174 (2018).
18. Han, H. et al. Rapid auxin-mediated phosphorylation of myosin regulates trafficking and polarity in *Arabidopsis*. Preprint at *bioRxiv* <https://doi.org/10.1101/2021.04.13.439603> (2021).
19. Haruta, M., Gray, W. M. & Sussman, M. R. Regulation of the plasma membrane proton pump (H⁺-ATPase) by phosphorylation. *Curr. Opin. Plant Biol.* **28**, 68–75 (2015).
20. Takahashi, K., Hayashi, K.-i. & Kinoshita, T. Auxin activates the plasma membrane H⁺-ATPase by phosphorylation during hypocotyl elongation in *Arabidopsis*. *Plant Physiol.* **159**, 632–641 (2012).
21. Yang, Z. et al. TMK-based cell surface auxin signaling activates cell wall acidification in *Arabidopsis*. *Nature* <https://doi.org/10.1038/s41586-021-03976-4> (2021).
22. Zhang, Y., Xiao, G., Wang, X., Zhang, X. & Friml, J. Evolution of fast root gravitropism in seed plants. *Nat. Commun.* **10**, 3480 (2019).
23. Kinoshita, T. & Shimazaki, K. Analysis of the phosphorylation level in guard-cell plasma membrane H⁺-ATPase in response to fusicoccin. *Plant Cell Physiol.* **42**, 424–432 (2001).
24. Yang, Y., Hammes, U. Z., Taylor, C. G., Schachtman, D. P. & Nielsen, E. High-affinity auxin transport by the AUX1 influx carrier protein. *Curr. Biol.* **16**, 1123–1127 (2006).
25. Serre, N. B. et al. AFB1 controls rapid auxin signalling through membrane depolarization in *Arabidopsis thaliana* root. *Nat. Plants* **7**, 1229–1238 (2021).
26. Prigge, M. J. et al. Genetic analysis of the *Arabidopsis* TIR1/AFB auxin receptors reveals both overlapping and specialized functions. *eLife* **9**, e54740 (2020).
27. Hayashi, K. et al. Rational design of an auxin antagonist of the SCF^{TIR1} auxin receptor complex. *ACS Chem. Biol.* **7**, 590–598 (2012).
28. Uchida, N. et al. Chemical hijacking of auxin signaling with an engineered auxin–TIR1 pair. *Nat. Chem. Biol.* **14**, 299–305 (2018).
29. Haruta, M., Sabat, G., Stecker, K., Minkoff, B. B. & Sussman, M. R. A peptide hormone and its receptor protein kinase regulate plant cell expansion. *Science* **343**, 408–411 (2014).

Publisher’s note Springer Nature remains neutral with regard to jurisdictional claims in published maps and institutional affiliations.

© The Author(s), under exclusive licence to Springer Nature Limited 2021

Methods

Plant materials and growth conditions

All *Arabidopsis* mutants and transgenic lines used are in the Columbia-0 (WT) background. The *pEB1b::EB1b-GFP*³⁰, *p35S::MAP4-GFP*³¹, *pSYP22::SYP22-YFP*³², *DR5::LUC*³³, *PM-Cyto*¹⁶ and *GCaMP3* (ref. ³⁴) marker lines have been described previously. The *tir1-10* (ref. ³⁵), *afb1-3* (ref. ²⁶), *tir1-1 afb2-1 afb3-1* (ref. ³⁶), *pTIR1::ccvTIR1 in tir1-1 afb2-3* (ref. ²⁸), *pTIR1::TIR1 in tir1-1 afb2-3* (which we call control for *ccvTIR1*)²⁸, *aux1-100* (ref. ³⁷), *cngc14-2* (ref. ¹⁴) and *fer-4* (ref. ²⁹) lines were donated by the authors of the original papers. The *pTIR1::TIR1-VENUS in tir1-1* (ref. ³⁸) and *pAFB1::AFB1-VENUS in afb1-3* (ref. ³⁹) lines were shared by S. Kepinski (University of Leeds). The *aha* mutants were the following: *aha2-5* (SALK_022010)⁴⁰, *aha1-7* (SALK_065288)⁴⁰ and *ost2-3D*⁴¹ (shared by A. Takemiya, Kyushu University). Two independent lines, *AtTAS1c-AHA#2* and *AtTAS1c-AHA#4*, were generated by J.C. and S.V. as follows: the syn-tasiRNA target sequence was inserted into pENTR-*AtTAS1c-B/c*⁴² using the hybridized TAS-AHA primer pair (Supplementary Table 4) and was recombined into pH7m24GW⁴³ together with pDONR P4-P1R⁴⁴ carrying the *PIN2* promoter²², to generate *pPIN2::AtTAS1c-AHA*. *pAHA2::AHA2-GFP*⁴⁵ seeds were donated by A.T. Fuglsang (University of Copenhagen). The *tmk* mutants were obtained as follows: *tmk3-2* (SALK_107741) was ordered from NASC, and T. Xu (Fujian Agriculture and Forestry University)^{8,46} kindly contributed *tmk1-1* (SALK_016360), *tmk2-1* (SAIL_1242_H07), *tmk4-1* (GABI_348E01), the complemented *pTMK1::gTMK1-FLAG in tmk1-1* and the *tmk1-1 tmk4-1 (tmk1,4)* double mutant. The *tmk1-1 tmk2-1 (tmk1,2)* and *tmk1-1 tmk3-2 (tmk1,3)* lines were generated by crosses using the above alleles. The transgenic plant lines carrying *DEX::TMK1-HA* and *DEX::TMK1^{K616R}-HA* were generated by H.R. and W.M.G. The *DEX::TMK1^{WT}-HA* construct (and those encoding *TMK1^{K616R}* or *TMK1^{K616E}*) were generated by cloning the corresponding *TMK1* cDNA without the stop codon (Supplementary Table 4) into pENTR/D-TOPO and subsequently recombining into the pBAV154 (ref. ⁴⁷) binary vector used in the Gateway system. The *pUBQ10::gTMK1-3HA* and *pTMK1::gTMK1-eGFP* lines were generated by amplifying the full-length genomic DNA for *TMK1* without the stop codon from WT genomic DNA using the primers indicated in Supplementary Table 4. *TMK1* genomic DNA was inserted into pDONR221 and subsequently recombined into pB7m34GW together with pDONR P4-P1R carrying the *UBQ10* or *TMK1* promoter and pDONR P2R-P3 3×HA or pDONR P2R-P3 eGFP. The constructs were transformed into *Agrobacterium tumefaciens* strain pGV3101 by electroporation and further into WT plants by floral dip.

Seeds were surface sterilized with chlorine gas, sown on half-strength Murashige and Skoog (½MS) medium supplemented with 1% (wt/vol) sucrose and 0.8% (wt/vol) phyto agar (pH 5.9), stratified in the dark at 4 °C for 2 d and then grown vertically at 21 °C with a long-day photoperiod (16 h light/8 h dark). Light sources used were Philips Green-Power LED production modules (in a deep red (660 nm)–far red (720 nm)–blue (455 nm) combination, Philips), with a photon density of 140.4 μmol m⁻² s⁻¹ ± 3%.

Treatment with inhibitors of gene translation (cycloheximide⁶) or transcription (cordycepin⁴⁸) was done with previously verified concentrations and durations.

Microfluidics

The microfluidic vRootchip was used mostly to analyse root tip growth and apoplastic pH in real time. Manufacturing of the chip, the sample preparation procedure and data analysis of root tip growth were performed as described previously⁶. Our new design contains an additional valve in the control layer that closes the ends of the root channels (Extended Data Fig. 1a). If air bubbles appear in the root channel, the additional valve allows the channel to be pressurized and air will be absorbed into the polydimethylsiloxane (PDMS) chip material within 2–10 min. After clearing any air bubbles, experiments started

after adaptation for at least 2 h. In addition, we introduced a graphical user interface (Supplementary Code 1) using Processing software (<https://processing.org/>) with the ControlIP5 package (<http://www.sojamo.de/libraries/controlIP5/>) that sends serial commands to the Arduino. A sketch (Supplementary Code 2) runs on the Arduino to operate the electronics and receive commands. A maximum of eight samples were used for each vRootchip. When comparing two genotypes, 3–4 seedlings were used for each genotype and mounted in alternating channels to minimize the time difference when imaging the two genotypes. For each root, we imaged one region of interest (ROI) containing early elongating epidermal cells and one ROI covering the root tip. As these two ROIs were captured sequentially, we imaged the apoplastic pH and growth of the same root close to simultaneously.

In vRootchip, we used basal liquid medium (¼MS + 0.1% sucrose, pH 5.8; adjusted with KOH). Media of different pH were prepared by adjusting the pH of basal medium with HCl or KOH. In addition, Ca²⁺-free liquid medium was prepared without CaCl₂.

Scanner growth assays

To complement the real-time imaging on vRootchip, growth analysis was performed on a vertical scanner that accommodates larger sample sizes, thereby allowing more conditions to be evaluated. We called this growth measurement ‘steady state’. Four-day-old seedlings were transferred to 60 mm × 15 mm petri dishes filled with 5 ml of ½MS medium with treatments as indicated. The petri dishes were placed on a vertically mounted flatbed scanner (Epson Perfection v.370), and seedlings were imaged through the layer of medium. Either wet black filter paper or ½MS medium containing activated charcoal was added to the lid to improve background contrast. The samples were automatically imaged every 10 or 30 min using the AutoIt script described previously⁴⁹, and scans were taken at 1,200 dpi. The resulting image series were analysed using StackReg stabilization and the Manual Tracking plugin in ImageJ or using the in-house-generated MATLAB-based application RootGrowth tracker⁵⁰.

Imaging and measuring apoplastic pH with HPTS dye

All apoplastic pH data were obtained using HPTS, a ratiometric fluorescent pH dye¹². pH measurements were performed both in the steady-state condition and in real-time vRootchip imaging. For steady-state pH analysis, 4-day-old seedlings were transferred to ½MS medium containing 1 mM HPTS (Thermo Scientific, 6358-69-6; dissolved in ddH₂O) and treatments were performed for 30 or 50 min. Subsequently, seedlings on a slice of the treatment medium were mounted in a Lab-Tek Chambered Coverglass.

Real-time imaging of apoplastic pH was done in vRootchip containing medium (¼MS + 0.1% sucrose) supplemented with 1 mM HPTS with or without treatment. All imaging was performed on the in-house-established vertical Zeiss LSM 800 confocal microscope¹⁵. Fluorescence signals for protonated HPTS (excitation, 405 nm; emission, 514 nm; visualized in red) and deprotonated HPTS (excitation, 488 nm; emission, 514 nm; visualized in green) were detected with a ×20/0.8 NA air objective. Image analysis was performed on a cropped region of elongating epidermal cells using batch processing from a previously described ImageJ macro¹². Relative pH was calculated as the background-subtracted intensity of the deprotonated dye divided by that of the protonated dye. Resulting relative pH data were plotted over time and statistically evaluated in GraphPad Prism 6. Note that we did not transform the relative pH values to absolute pH values, which would have required the generation of a calibration curve for each experiment.

Imaging and measuring cytosolic pH with the PM-cyto reporter

Real-time imaging of the cytosolic pH near the PM was done by using the *PM-Cyto* reporter line¹⁶ in vRootchip and a vertical Zeiss LSM 800

confocal microscope¹⁵. Signal from sequential illumination at 488 and 405 nm with emission at 514 nm for both, corresponding to the two absorption peaks of pHluorin, was detected with a $\times 20/0.8$ NA air objective. For each root in vRootchip, two ROIs were tracked over time, one containing elongating epidermal cells for measuring the cytosolic pH and the other covering the root tip for measuring the root growth rate. Image analysis was performed similarly to that for HPTS described above.

Imaging microtubule orientation, vacuolar morphology and cytosolic Ca^{2+} spikes

The *pEB1b::EB1b-GFP* marker line³⁰ was used to track the dynamics of CMT orientation in vRootchip. Images were obtained every 6.25 s, and analysis of CMT orientation was performed in ImageJ by maximum z projection on every 10 frames and quantification with a modified version of the Fibril Tool macro for batch processing⁵¹. The *p35S::MAP4-GFP* marker line³¹ was used to capture CMT orientation after treatment for the indicated time period (steady state). The CMT orientation angle was calculated using the Bioline script¹⁰. For both marker lines, the GFP (excitation, 488 nm; emission, 514 nm) signal was detected by Plan-Apochromat $\times 20/0.8$ NA air objective in the vertical Zeiss LSM 800 confocal microscope¹⁵.

The *pSYP22::SYP22-YFP* marker line³² was used for imaging vacuolar morphology. We used a mounting system⁵², which allows injection of new liquid medium during imaging. Images were acquired before and 30 min after mock treatment or treatment with 100 nM IAA, and the YFP (excitation, 488 nm; emission, 527 nm) intensity was detected with a C-Apochromat $\times 40/1.20$ NA W Korr objective in an inverted Zeiss LSM 800 confocal microscope.

The *GCaMP3* marker line³⁴ was crossed with the *ccvTIR1* and control transgenic lines²⁸, with the resulting lines used for imaging cytosolic Ca^{2+} levels in vRootchip. Images were acquired every 14.4 s for 1 h. GFP (excitation, 488 nm; emission, 514 nm) signal was detected with a Plan-Apochromat $\times 20/0.8$ NA air objective in the vertical Zeiss LSM 800 confocal microscope¹⁵.

Non-invasive microelectrode (MIFE) ion flux measurements

Net fluxes of H^+ , K^+ and Ca^{2+} were measured using the non-invasive microelectrode ion flux estimation (MIFE) technique essentially as described elsewhere⁵³. In brief, microelectrodes were pulled with a PE-22 puller (Narishige), dried in an oven and silanized with tributylchlorosilane (Sigma-Aldrich, 90794). The prepared electrode blanks were backfilled with the corresponding solutions for each measured ion, and the electrode tips were front-filled with selective liquid ion exchangers (LIXs; purchased from Sigma-Aldrich) to measure the ions of interest (H^+ , 95291; K^+ , 99311; Ca^{2+} , 99310). Roots from intact 6-day-old *Arabidopsis* WT seedlings were immobilized in a measuring chamber using Perspex holders with addition of basic salt medium (BSM; 0.5 mM KCl and 0.1 mM CaCl_2 , pH 5.8; unbuffered). Measurements were recorded from elongating epidermal cells (~ 450 μm from the root tip). After 40 min of conditioning, the microelectrodes were positioned 20 μm from the root surface and moved in a slow (6-s cycle, 100- μm amplitude) square wave by a computer-driven micromanipulator (Narishige, MHW-4). Net ion fluxes were calculated by MIFEFLUX software on the basis of the measured difference in electrochemical gradient between the two positions using cylindrical diffusion geometry as described elsewhere⁵³. Steady-state fluxes were recorded for 5–10 min to make sure that the steady-state condition was reached. Then, 10 nM IAA was applied to the measuring chamber, and transient H^+ , K^+ and Ca^{2+} kinetics were measured for a further 20 min. At least nine individual plants from several batches were used. The sign convention was 'influx positive'.

Membrane potential measurements

Membrane potential (MP) was measured for elongating root epidermal cells from intact *Arabidopsis* seedlings. Conventional microelectrodes

(Harvard Apparatus) were filled with 1 M KCl and connected to the MIFE electrometer via the Ag/AgCl half-cell. During MP measurement, a microelectrode with a tip diameter of 0.5 μm was manually impaled into the elongating epidermal cells (~ 450 μm from the root tip) using a 3D micromanipulator (Narishige, MHW-4). MP values were recorded by MIFE CHART software for at least 2 min after stabilization⁵³. Before measurements, a 6-day-old seedling was immobilized on a Perspex block using Parafilm strips, and the block was inserted into a vertical Perspex measuring chamber and filled with BSM of the required pH. After 40 min of conditioning in BSM, the measuring chamber was mounted on a MIFE microscope stage located in a Faraday cage for MP measurements. MP measurements were conducted in two ways: under steady-state conditions (at different pH values) and as transient kinetics (in response to IAA application). In the steady-state experiments, MP values were recorded from the roots of 5–6 individual seedlings, with a new electrode used for each measurement to ensure that the electrode tip was not blocked. At least four measurements were made for each seedling. In transient kinetics experiments, MP was recorded from a root in BSM (pH 5.8) for 1–2 min after initial cell penetration and IAA prepared in BSM was then added to the chamber (final concentration, 10 nM) followed by MP recording for 5 min.

Evaluating the TIR1 transcriptional response using the *DRS::LUC* line

Four-day-old *DRS::LUC* seedlings³³ were placed on the surface of solidified $\frac{1}{2}$ MS medium with 200 μl of 5 mM D-luciferin dissolved in a $1\times$ PBS drop on the root tips for 30 min as pretreatment. Subsequently, the samples were transferred to solidified $\frac{1}{2}$ MS medium supplemented with mock treatment solution, 10 nM IAA, 10 μM FC or IAA + FC and immediately imaged in an in-house-established dark box with a Photometric Evolve EMCCD camera equipped with a 17-mm fixed lens/0.95 and an additional 125-mm lens⁴⁹. The multiplier EMCCD gain was set to 70 s, the exposure time was set to 35 s and images were acquired every 2 min. The resulting time-lapse video was analysed in ImageJ as described previously⁴⁹.

Identification of TMK1-interacting proteins using IP with MS/MS

IP experiments were performed in three biological replicates as described previously⁵⁴ using 1 g of roots from 7-day-old seedlings from the *pTMK1::TMK1-eGFP* transgenic line and 1 g of roots from WT seedlings. Interacting proteins were isolated by incubating total protein extracts with 100 μl of anti-GFP-coupled magnetic beads (Milenyi Biotec). Three replicates of *pTMK1::TMK1-eGFP* were compared with three WT replicates. MS/MS on a Q-Exactive device (Thermo Fisher) and statistical analysis using MaxQuant and Perseus software were performed as described previously⁵⁵.

Identification of TIR1- and AFB1-interacting proteins using IP and MS/MS

For IP, ground plant material from *pTIR1::TIR1-VENUS* in *tir1-1* and *pAFB1::AFB1-VENUS* in *afb1-3* transgenic lines was lysed in mild lysis buffer (50 mM Tris pH 7.5, 150 mM NaCl, 2 mM MgCl_2 , 0.2 mM EDTA, $1\times$ CPI, 0.5 mM DTT, 0.2% NP-40 and 1 mg ml^{-1} DNase) and mildly sonicated using a Bioruptor (Diagenode). After lysate clearance, supernatant was subjected to enrichment using GFP-Trap agarose beads (Chromotek) for 45 min at 4 $^{\circ}\text{C}$ with gentle rotation. Beads were subsequently washed twice in lysis buffer, twice in detergent-free lysis buffer and three times in 50 mM ammonium bicarbonate (ABC) (Sigma) with centrifugation between washes at 2,000g for 2 min at 4 $^{\circ}\text{C}$. After the final wash, bead-precipitated proteins were alkylated using 50 mM acrylamide (Sigma). Precipitated proteins were subjected to on-bead trypsinization using 0.35 μg of trypsin (Roche) per reaction. After overnight incubation at 25 $^{\circ}\text{C}$, peptides were desalted and concentrated using C18 StageTips.

After Stagetip processing, peptides were applied to online nanoLC–MS/MS using a 60-min 8–50% acetonitrile gradient. Spectra were recorded on an LTQ-XL mass spectrometer (Thermo Scientific), and statistical analysis using MaxQuant and Perseus software was performed as described previously⁵⁵.

Phosphoproteomics of auxin-treated roots

Roots from 5-day-old plants were treated and immediately harvested and flash frozen in liquid nitrogen. They were then ground to fine powder in liquid nitrogen. Powder was suspended in SDS lysis buffer (100 mM Tris pH 8.0, 4% SDS and 10 mM DTT) and sonicated using a cooled Bioruptor (Diagenode) for 10 min with high power and a 30-s on/30-s off cycle. Lysate was cleared by centrifugation at maximum speed for 30 min. Protein concentrations were determined using Bradford reagent (Bio-Rad).

In filter-aided sample preparation, Amicon filter units with a 30-kDa molecular weight cut-off (Merck Millipore) were used. Filters were first tested by applying 50 µl of UT buffer (8 M urea and 100 mM Tris pH 8.5) and centrifuging at 11,000 r.p.m. for 10 min at 20 °C. The desired amount of protein sample was next mixed with UT buffer to a final volume of 200 µl, applied to the filter and centrifuged for 15 min. All centrifuge steps were at 11,000 r.p.m. at 20 °C. The filter was washed with UT buffer for 15 min. Retained proteins were alkylated with 50 mM acrylamide (Sigma) in UT buffer for 30 min at 20 °C while gently shaking followed by a triple-wash step with UT buffer for 15 min and three washes with 50 mM ABC buffer. After the last wash, proteins were cleaved by adding trypsin (Roche) in a 1:100 trypsin to protein ratio. Digestion was performed overnight. The following day, the filter was changed to a new tube and peptides were eluted by centrifuging for 15 min. Further elution was performed twice by adding 50 mM ABC buffer and centrifuging at 11,000 r.p.m. for 10 min at 20 °C.

For peptide desalting and concentration, 200-µl tips were fitted with two plugs of C18 octadecyl 47-mm disc 2215 (Empor) material as well as 1 mg of LiChroprep RP-18 (Merck) for every 10 µg of peptide. Tips were sequentially equilibrated with 100% methanol, with 80% acetonitrile in 0.1% formic acid and twice with 0.1% formic acid for 4 min at 1,500g. After equilibration, peptides were loaded for 20 min at 400g. Bound peptides were washed with 0.1% formic acid and eluted with 80% acetonitrile in 0.1% formic acid for 4 min at 1,500g. Eluted peptides were subsequently concentrated using a vacuum concentrator for 30 min at 45 °C and resuspended in 50 µl of 0.1% formic acid.

For phosphopeptide enrichment, magnetic Ti⁴⁺-IMAC (MagResyn) microparticles were used according to the manufacturer's protocol. Enrichments were performed with 1 mg of peptide in biological quadruplicate.

After Stagetip processing, peptides were applied to online nanoLC–MS/MS using a 120-min 8–50% acetonitrile gradient for phosphoproteomics. Spectrum recording and statistical analysis were as previously described, with the addition of phosphorylation as a variable modification⁵⁵. Filtering of datasets was performed in Perseus as described previously⁵⁶.

Phosphoproteomics in WT and *tmk1-1* roots

Four biological replicates of WT and *tmk1-1* roots were prepared and treated as indicated. They were subjected to the phosphoproteomic pipeline^{55,56}, and differentially phosphorylated peptides belonging to H⁺-ATPases were specifically filtered out of the big dataset (Supplementary Table 1).

In vitro kinase assay with [γ -³²P]ATP

6×His–MBP–TMK1^{WT} kinase domain (or kinase-dead TMK1^{K616E}) was purified from *Escherichia coli*. In brief, approximately 100 ng of purified protein was added to reactions containing 5 mM HEPES pH 7.5, 10 mM MgCl₂, 10 mM MnCl₂ and 1 mM DTT and the assay was initiated by adding 1 µl of ATP solution containing 100 µM (unlabelled) ATP and 33 nM [γ -³²P]

ATP (3,000 Ci mmol⁻¹). Approximately 150 ng of purified GST–AHA2 C-terminal domain was added as indicated. Reactions were incubated at 28 °C for 40 min, stopped with SDS–PAGE sample buffer and run on SDS–PAGE gels; phosphorylation was visualized by autoradiography. Ponceau staining was performed as a loading control.

Protein extraction and western blot analysis for co-IP and determination of AHA2 phosphorylation state

To isolate PM H⁺-ATPases and potential interactors, 5- to 7-day-old plant roots were harvested at the indicated time points after treatment with 10 or 100 nM IAA. Twenty-four hours before evaluation of auxin effects, the seedlings were sprayed with ½AM solution containing 30 µM kynurenine. Root samples were flash frozen in liquid nitrogen and ground (Retsch mill, twice for 1 min at 20 Hz). Root powder was then suspended at a 1:1 (wt/vol) ratio in protein extraction buffer (25 mM Tris–HCl pH 7.5, 150 mM NaCl, 1% Triton X-100, 1× Roche cOmplete Protease Inhibitor Cocktail, 1× Roche PhosSTOP, 1 mM EDTA, 1 mM DTT and 0.5 mM PMSF). Samples were incubated on ice for 30 min, followed by a centrifugation step at 10,000g to discard the plant debris. The cleared supernatant containing the proteins of interest was collected, and total protein content was determined using Quick Start Bradford reagent (Bio-Rad). The prepared samples could further be used for co-IP or SDS–PAGE analysis. In order not to lose relevant proteins, protein samples were not boiled in the presence of reducing Laemmli buffer and no harsher PM extraction or membrane enrichment was attempted.

For co-IP, root extracts (obtained by extraction in the lysis buffer supplied in the Miltenyi µMACs kit supplemented with 1× Roche cOmplete Protease Inhibitor Cocktail, 1 mM DTT and 0.5 mM PMSF) were incubated with magnetic beads from the Miltenyi anti-GFP, anti-HA or anti-FLAG µMACs kit (depending on the tags of the proteins of interest) and kept rotating for 4 h at 4 °C. Elution was performed with room-temperature denaturing elution buffer, and the proteins were analysed by SDS–PAGE and western blot analysis.

Following separation of proteins by SDS–PAGE in a 10% acrylamide gel (Protein TGX, Bio-Rad), proteins were transferred to PVDF membranes by electroblotting (Trans-blot Turbo, Bio-Rad). The membranes were then incubated in blocking buffer (0.05% Tween-20, 5% milk powder or 3% BSA, 20 mM Tris–HCl pH 7.5 and 150 mM NaCl) for at least 60 min and incubated with antibody solution against the protein of interest. All raw images for blots are provided in Supplementary Fig. 1.

Antibodies

The anti-AHA2 and anti-pThr947 AHA2 antibodies were shared by T.K. and were used as described previously⁵⁷ at a final dilution of 1:5,000 in TBST + 3% BSA, followed by anti-rabbit IgG secondary antibody conjugated to horseradish peroxidase (HRP) (GE Healthcare, NA934) at a dilution of 1:10,000 and chemiluminescence reaction (SuperSignal West Femto, Thermo Scientific). To allow detection with multiple antibodies on the same PVDF membrane, mild stripping was performed using buffer containing 15 g L⁻¹ glycine, 1 g L⁻¹ SDS and 10 ml L⁻¹ Tween-20 at pH 2.2 for 2–5 min.

ATP hydrolysis in root samples

To deplete endogenous auxin levels in seedlings, 14-day-old plants were pretreated with 30 µM kynurenine for 24 h in the dark. Then, the pretreated seedlings were incubated in the presence or absence of 100 nM IAA for 60 min in the dark. Roots excised from the seedlings were homogenized in homogenization buffer (50 mM MOPS–KOH pH 7.0, 100 mM KNO₃, 2 mM sodium molybdate, 0.1 mM NaF, 2 mM EGTA, 1 mM PMSF and 20 µM leupeptin), and the homogenates were centrifuged at 10,000g for 10 min. The obtained supernatant was further ultra-centrifuged at 45,000 r.p.m. for 60 min. The resultant precipitate (microsomal fraction) was resuspended in homogenization buffer. ATP hydrolytic activity in the microsomal fraction was determined by measuring vanadate-sensitive release of inorganic phosphate from ATP

following a published method⁵⁸ with the following modifications. The microsomal fraction (22.5 μ l, 0.2 mg ml⁻¹) was mixed with an equal volume of reaction buffer (60 mM MES-Tris pH 6.5, 6 mM MgSO₄, 200 mM KNO₃, 1 mM ammonium molybdate, 10 μ g ml⁻¹ oligomycin, 2 mM NaN₃, 0.1% Triton X-100, 1 mM PMSF and 20 μ M leupeptin) with or without 1 μ l of 10 mM sodium orthovanadate. The reaction was started by adding 5 μ l of 2 mM ATP and terminated by adding 50 μ l of the stop solution (2.6% (wt/vol) SDS, 0.5% (wt/vol) sodium molybdate and 0.6N H₂SO₄) after incubating at 30 °C for 30 min.

Bimolecular fluorescence complementation

Following a previously described method³, the full-length coding sequences of AHA2 and TMK1 without stop codons were amplified by PCR (primers listed in Supplementary Table 4), cloned into pENTR/D-TOPO or pDONR207 and recombined into pSPYNE and pSPYCE⁵⁹ to generate BiFC expression constructs. The resulting binary vectors were introduced into *Agrobacterium* GV3101 by electroporation, and cells were cultured to an OD₆₀₀ of 0.8. Syringe infiltration was performed in *N. benthamiana* leaves as described previously⁶⁰. For the constructs of interest, a final OD₆₀₀ of 0.2 was used and p19 was co-infiltrated at an OD₆₀₀ of 0.1 to avoid gene silencing. Infiltration buffer of pH 5.8 contained 10 mM MgSO₄, 10 mM MES-KOH and 0.15 mM acetosyringone. TMK1 overexpression, even when transient, has a strong effect on the viability of leaves, so samples were taken daily after infiltration to determine the optimal balance between expression level and viable leaf cells. To avoid this effect, TMK1^{K616R} was expressed and still interacted with AHA2, while no interaction was observed with AUX1 (Extended Data Fig. 4g). The absence of an interaction between expressed AHA2 and AUX1 was previously reported in the same system^{61,62} (Extended Data Fig. 4g). To visualize protein interactions, sections of the leaves were imaged using a Zeiss LSM 700 confocal microscope.

Quantitative RT-PCR

RNA was extracted from 5-day-old light-grown root tips with the RNeasy Plant Mini kit (Qiagen), with three biological replicates for each genotype. Two micrograms of RNA was used for cDNA synthesis (Qiagen). Samples were pipetted in three technical replicates using an automated JANUS Workstation (PerkinElmer) and measured on a Roche Real-Time PCR LightCycler 480 using Luna Universal qPCR Master Mix (NEB, M3003S). Primers used to assess gene expression are listed in Supplementary Table 4. Expression levels were normalized to those for *ELONGATION FACTOR 1 ALPHA* (At5G60390)⁶³.

Statistical analysis and reproducibility

All graphs were generated using GraphPad Prism 6 or 8. For statistical analysis of vRootchip data, two-way ANOVA was performed for the entire timeframe of the experiment, except when a specific time interval is indicated. Welch ANOVA was applied for the scanner growth assay with multiple time points, and one-way ANOVA was used for steady-state (one incubation time point) pH and scanner growth datasets. Asterisks indicate significant differences on all graphs with NS for $P > 0.05$; * $P \leq 0.05$, ** $P \leq 0.01$, *** $P \leq 0.001$ and **** $P \leq 0.0001$. Experiments always included sufficient biological replicates and were repeated at least twice independently with similar results. The depicted data show the results from one representative experiment.

Reporting summary

Further information on research design is available in the Nature Research Reporting Summary linked to this paper.

Data availability

The data and full blots are available within the paper and its Supplementary Information. Source data are provided with this paper.

Code availability

All codes used in the manuscript are provided in the Supplementary Information.

- Komaki, S. et al. Nuclear-localized subtype of end-binding 1 protein regulates spindle organization in *Arabidopsis*. *J. Cell Sci.* **123**, 451–459 (2010).
- Marc, J. et al. A GFP-MAP4 reporter gene for visualizing cortical microtubule rearrangements in living epidermal cells. *Plant Cell* **10**, 1927–1939 (1998).
- Robert, S. et al. Endosidin1 defines a compartment involved in endocytosis of the brassinosteroid receptor BRI1 and the auxin transporters PIN2 and AUX1. *Proc. Natl Acad. Sci. USA* **105**, 8464–8469 (2008).
- Moreno-Risueno, M. A. et al. Oscillating gene expression determines competence for periodic *Arabidopsis* root branching. *Science* **329**, 1306–1311 (2010).
- Toyota, M. et al. Glutamate triggers long-distance, calcium-based plant defense signaling. *Science* **361**, 1112–1115 (2018).
- Parry, G. et al. Complex regulation of the TIR1/AFB family of auxin receptors. *Proc. Natl Acad. Sci. USA* **106**, 22540–22545 (2009).
- Dharmasiri, N. et al. Plant development is regulated by a family of auxin receptor F box proteins. *Dev. Cell* **9**, 109–119 (2005).
- Swarup, R. et al. Structure–function analysis of the presumptive *Arabidopsis* auxin permease AUX1. *Plant Cell* **16**, 3069–3083 (2004).
- Wang, R. et al. HSP90 regulates temperature-dependent seedling growth in *Arabidopsis* by stabilizing the auxin co-receptor F-box protein TIR1. *Nat. Commun.* **7**, 10269 (2016).
- Rast-Somssich, M. I. et al. The *Arabidopsis* JAGGED LATERAL ORGANS (JLO) gene sensitizes plants to auxin. *J. Exp. Bot.* **68**, 2741–2755 (2017).
- Haruta, M. et al. Molecular characterization of mutant *Arabidopsis* plants with reduced plasma membrane proton pump activity. *J. Biol. Chem.* **285**, 17918–17929 (2010).
- Yamauchi, S. et al. The plasma membrane H⁺-ATPase AHA1 plays a major role in stomatal opening in response to blue light. *Plant Physiol.* **171**, 2731–2743 (2016).
- Carbonell, A. et al. New generation of artificial microRNA and synthetic trans-acting small interfering RNA vectors for efficient gene silencing in *Arabidopsis*. *Plant Physiol.* **165**, 15–29 (2014).
- Karimi, M., Bley, A., Vanderhaeghen, R. & Hilson, P. Building blocks for plant gene assembly. *Plant Physiol.* **145**, 1183–1191 (2007).
- Marquès-Bueno, M. M. et al. A versatile multisite Gateway-compatible promoter and transgenic line collection for cell type-specific functional genomics in *Arabidopsis*. *Plant J.* **85**, 320–333 (2016).
- Fuglsang, A. T. et al. Receptor kinase-mediated control of primary active proton pumping at the plasma membrane. *Plant J.* **80**, 951–964 (2014).
- Wang, Q. et al. A phosphorylation-based switch controls TAA1-mediated auxin biosynthesis in plants. *Nat. Commun.* **11**, 679 (2020).
- Lee, J. et al. Type III secretion and effectors shape the survival and growth pattern of *Pseudomonas syringae* on leaf surfaces. *Plant Physiol.* **158**, 1803–1818 (2012).
- Robert, S. et al. ABP1 mediates auxin inhibition of clathrin-dependent endocytosis in *Arabidopsis*. *Cell* **143**, 111–121 (2010).
- Li, L., Krens, S. G., Fendrych, M. & Friml, J. Real-time analysis of auxin response, cell wall pH and elongation in *Arabidopsis thaliana* hypocotyls. *Bio. Protoc.* **8**, e2685 (2018).
- Gelová, Z. et al. Developmental roles of auxin binding protein 1 in *Arabidopsis thaliana*. *Plant Sci.* **303**, 110750 (2021).
- Boudaoud, A. et al. FibrilTool, an ImageJ plug-in to quantify fibrillar structures in raw microscopy images. *Nat. Protoc.* **9**, 457–463 (2014).
- Narasimhan, M. et al. Systematic analysis of specific and nonspecific auxin effects on endocytosis and trafficking. *Plant Physiol.* **186**, 1122–1142 (2021).
- Shabala, S. N., Newman, I. A. & Morris, J. Oscillations in H⁺ and Ca²⁺ ion fluxes around the elongation region of corn roots and effects of external pH. *Plant Physiol.* **113**, 111–118 (1997).
- De Rybel, B. et al. A bHLH complex controls embryonic vascular tissue establishment and indeterminate growth in *Arabidopsis*. *Dev. Cell* **24**, 426–437 (2013).
- Wendrich, J. R., Boeren, S., Möller, B. K., Weijers, D. & De Rybel, B. in *Plant Hormones*. 147–158 (Springer, 2017).
- Nikonov, N. et al. Early mannitol-triggered changes in the *Arabidopsis* leaf (phospho) proteome reveal growth regulators. *J. Exp. Bot.* **69**, 4591–4607 (2018).
- Hayashi, Y. et al. Biochemical characterization of in vitro phosphorylation and dephosphorylation of the plasma membrane H⁺-ATPase. *Plant Cell Physiol.* **51**, 1186–1196 (2010).
- Inoue, S., Takahashi, K., Okumura-Noda, H. & Kinoshita, T. Auxin influx carrier AUX1 confers acid resistance for *Arabidopsis* root elongation through the regulation of plasma membrane H⁺-ATPase. *Plant Cell Physiol.* **57**, 2194–2201 (2016).
- Walter, M. et al. Visualization of protein interactions in living plant cells using bimolecular fluorescence complementation. *Plant J.* **40**, 428–438 (2004).
- Leuzinger, K. et al. Efficient agroinfiltration of plants for high-level transient expression of recombinant proteins. *J. Vis. Exp.* **77**, <https://doi.org/10.3791/50521> (2013).
- Ren, H., Park, M. Y., Spartz, A. K., Wong, J. H. & Gray, W. M. A subset of plasma membrane-localized PP2C.D phosphatases negatively regulate SAUR-mediated cell expansion in *Arabidopsis*. *PLoS Genet.* **14**, e1007455 (2018).
- Wong, J. H., Spartz, A. K., Park, M. Y., Du, M. & Gray, W. M. Mutation of a conserved motif of PP2C.D phosphatases confers SAUR immunity and constitutive activity. *Plant Physiol.* **181**, 353–366 (2019).
- Czechowski, T., Stitt, M., Altmann, T., Udvardi, M. K. & Scheible, W.-R. Genome-wide identification and testing of superior reference genes for transcript normalization in *Arabidopsis*. *Plant Physiol.* **139**, 5–17 (2005).
- Dumont, J. N. Oogenesis in *Xenopus laevis* (Daudin). I. Stages of oocyte development in laboratory maintained animals. *J. Morphol.* **136**, 153–179 (1972).

Article

Acknowledgements We thank N. Gnyliukh and L. Hörmayer for technical assistance and N. Paris for sharing *PM-Cyto* seeds. We gratefully acknowledge the Life Science, Machine Shop and Bioimaging Facilities of IST Austria. This project has received funding from the European Research Council Advanced Grant (ETAP-742985) and the Austrian Science Fund (FWF) under I 3630-B25 to J.F., the National Institutes of Health (GM067203) to W.M.G., the Netherlands Organization for Scientific Research (NWO; VIDI-864.13.001), Research Foundation-Flanders (FWO; Odysseus II GOD0515N) and a European Research Council Starting Grant (TORPEDO-714055) to W.S. and B.D.R., the VICI grant (865.14.001) from the Netherlands Organization for Scientific Research to M.R. and D.W., the Australian Research Council and China National Distinguished Expert Project (WQ20174400441) to S.S., the MEXT/JSPS KAKENHI to K.T. (20K06685) and T.K. (20H05687 and 20H05910), the European Union's Horizon 2020 research and innovation programme under Marie Skłodowska-Curie grant agreement no. 665385 and the DOC Fellowship of the Austrian Academy of Sciences to L.L., and the China Scholarship Council to J.C.

Author contributions L.L., I.V. and J.F. conceived and designed the experiments. L.L. and I.V. carried out most of the experiments and analysis. M.R. and D.W. performed the phosphoproteomics analysis and TIR1/AFB1 IP-MS/MS. I.V., W.S. and B.D.R. performed TMK1 IP-

MS/MS experiments and statistical analysis. MS/MS analysis was performed by the VIB Proteomics Core. L.S. and S.S. performed MIFE experiments. K.T. and T.K. performed the ATP hydrolysis assays. J.C. and S.V. created and shared the *AtTAS1c-AHA* lines. L.R. and L.L. created transgenic lines and crosses. H.R. and W.M.G. conducted [γ - 32 P]ATP kinase assays and leaf wilting phenotype analysis, shared plasmids and seed materials, and contributed to discussion of the results. J.M. and L.L. modified the microfluidic chip. L.L., I.V. and J.F. wrote the manuscript.

Competing interests The authors declare no competing interests.

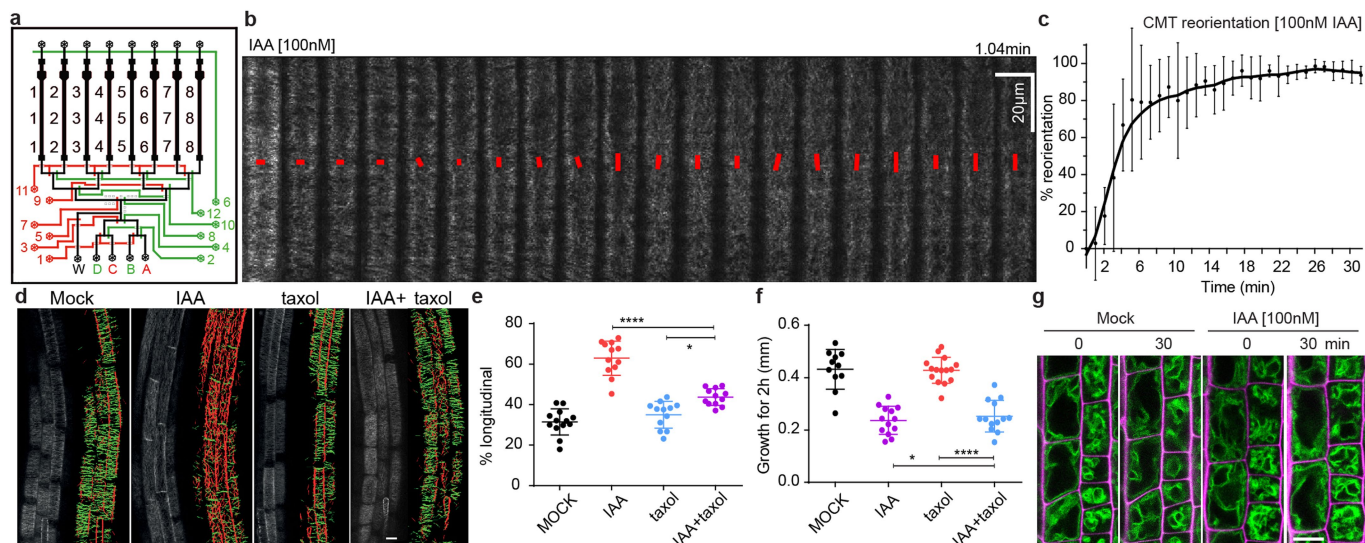
Additional information

Supplementary information The online version contains supplementary material available at <https://doi.org/10.1038/s41586-021-04037-6>.

Correspondence and requests for materials should be addressed to Inge Verstraeten or Jiří Friml.

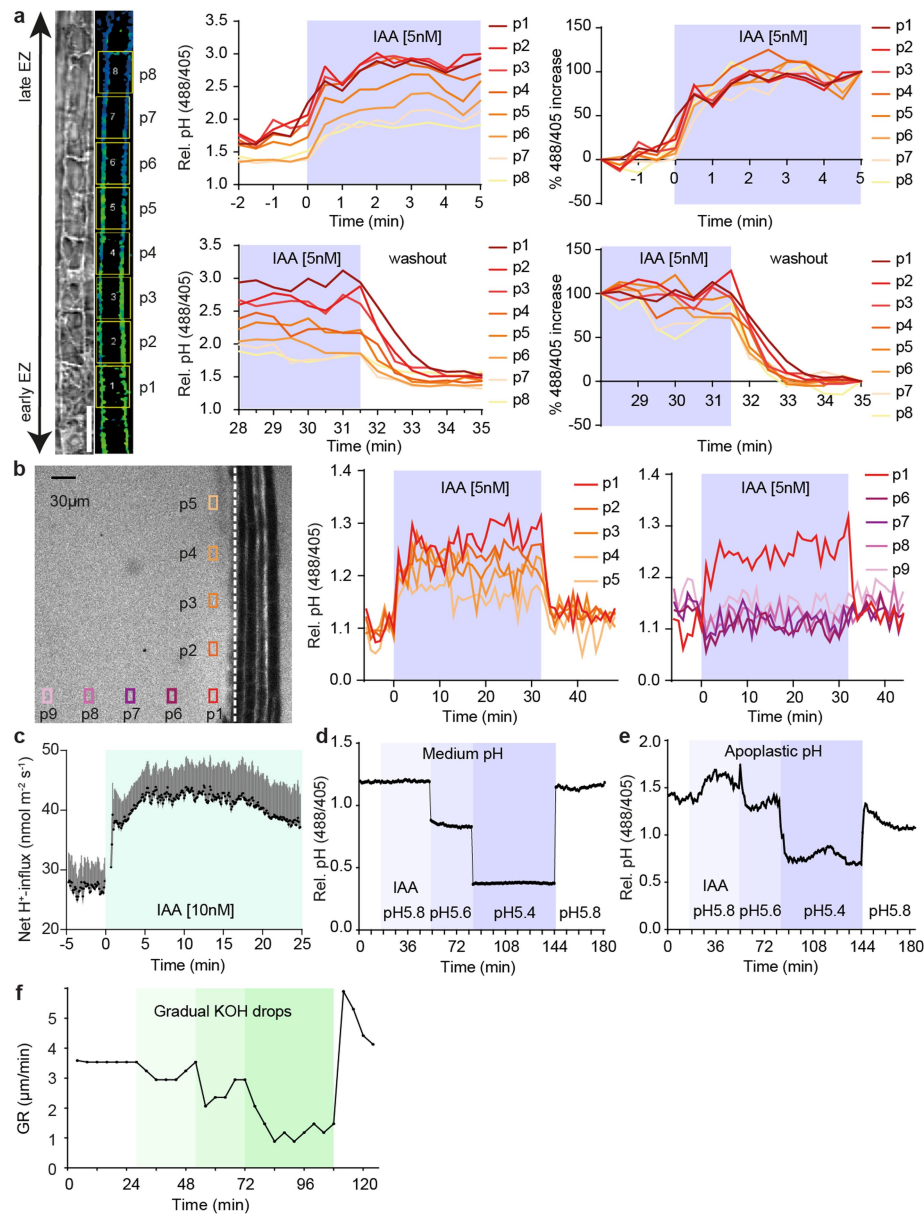
Peer review information *Nature* thanks Malcolm Bennett, Anthony Bishopp and the other, anonymous, reviewer(s) for their contribution to the peer review of this work. Peer reviewer reports are available.

Reprints and permissions information is available at <http://www.nature.com/reprints>.



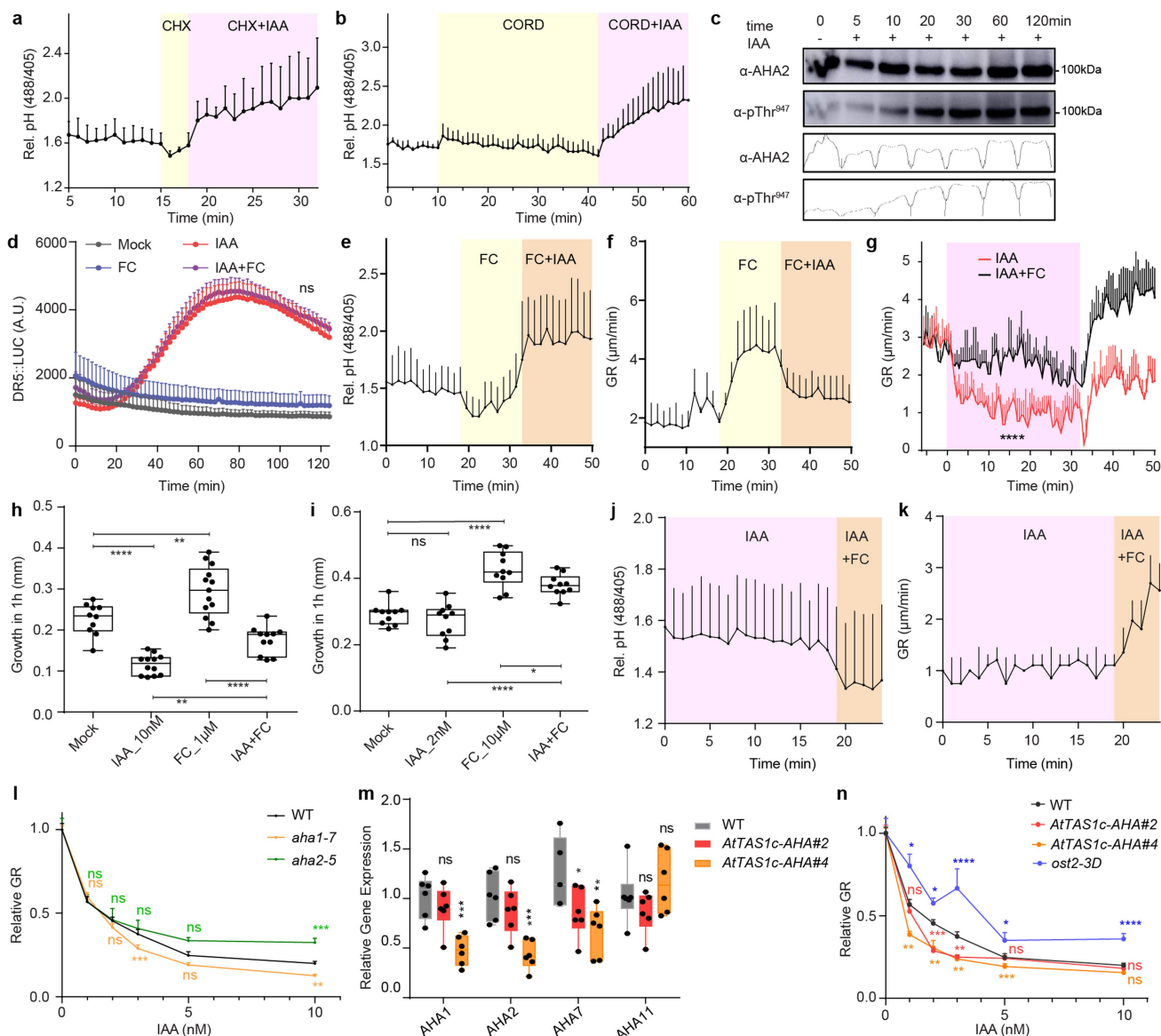
Extended Data Fig. 1 | Investigation of CMT and vacuolar morphology in auxin-induced rapid root growth inhibition. **a**, Scheme of the modified vRootchip, with added valve 6 and adjusted valve routes. **b, c**, Dynamic cortical microtubule (CMT) transversal to longitudinal reorientation in response to 100nM IAA treatment. CMT were imaged at 6.25s intervals in elongating root epidermal cells in the *pEB1b::EB1b-GFP* marker line in vRootchip. Max Z-projection of 10 subsequent time frames was analysed using the FibrilTool. Average orientation of CMT is represented by the slope of the red line and the length of the line represents its anisotropy (**b**). (**c**) Quantification of CMT reorientation as in **b**. CMT reorientation at every time point is calculated as the difference in angle of that time point minus the initial time point angle divided by the difference in the angles of the initial time point and end time point (42min). Mean of 5 elongating cells \pm s.d. (**c**). **d-f**, Analysis of CMT reorientation

in elongating root epidermal cells (**d, e**) and root growth (**f**) of *p35S::MAP4-GFP* in response to 10nM IAA, 10µM taxol and IAA+taxol co-treatment. CMT orientation was analysed with the Bioline script. Green-colored CMTs mark transversal oriented CMT (angle between -45° and $+45^\circ$), while red-colored CMTs indicate longitudinal orientation (angle between $+45^\circ$ and 135°). Scale bar=15µm (**d**). Percentage of longitudinal CMT. $n>11$ roots, One-way ANOVA (**e**). Growth on respective treatments after 2h. $n>10$ roots. Box plots depicts minimum to maximum, mean \pm s.d. One-way ANOVA without modifications for multiple comparison (**f**). * $P\leq 0.05$, **** $P\leq 0.0001$. **g**, Vacuolar morphology tracked using *pSYP22::SYP22-YFP* (green signal) in elongating cells before and after 30min of 100nM IAA. Scale bar=15µm. Magenta signal represents propidium-iodide stained cell walls.



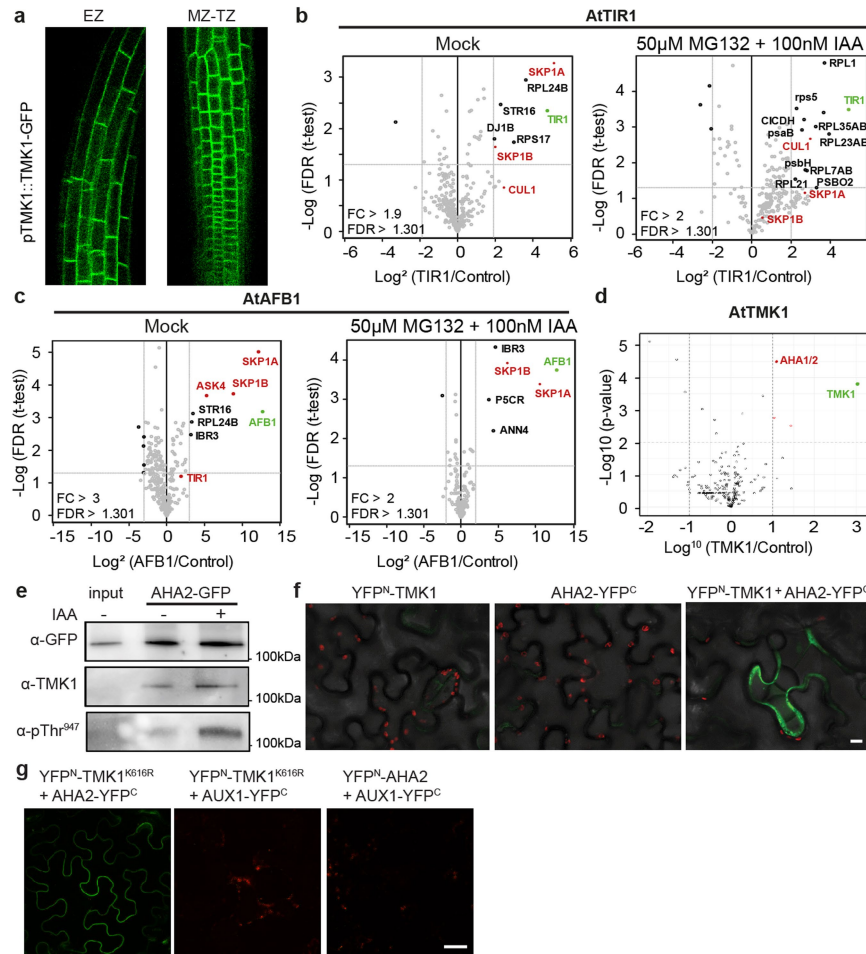
Extended Data Fig. 2 | Apoplastic pH in auxin-induced rapid root growth inhibition. **a**, Apoplastic pH dynamics measured across the whole EZ (p1-p8) in vRootchip. The TL and blue-yellow scale image are from the same sample shown in Fig. 1a. Scale bar=30 μm . The upper charts depict apoplastic pH in the indicated cells in response to 5nM IAA, and the lower charts represent the pH in response to washout. The right two charts show the speed at which each cell reaches its maximum pH change calculated as the difference between pH at a given time point and pre-stimulus pH, divided by the final pH change. **b**, Dynamics of root surface pH and medium pH in vRootchip. The left graph shows the elongation zone of the root. ROIs p1-p5 were chosen vertically along the root, 30 μm away from the root surface indicated by the vertical white dotted line, while ROIs p6-p9 were distanced horizontally away from the root.

The pH at the surface of the root (p1-p5) increased after IAA and recovered within 30s after washout. In contrast, the pH away from the root surface did not change significantly (p6-p9). **c**, H^+ -net influx measured by a non-invasive microelectrode before and after 10nM IAA treatment in the elongating zone of WT roots. Mean of 9 roots+s.e.m. **d**, **e**, Changes in medium pH (**d**) and apoplastic pH (**e**) after different medium pH exchanges in vRootchip. Sequentially used media: basal medium at pH 5.8, auxin-containing medium at pH 5.8, more acidic medium of pH 5.6, followed by pH 5.4 and again basal medium at pH 5.8. **f**, Quantification of root growth in response to gradual addition of KOH in the medium in the vRootchip. The greener the shade, the more KOH was added and followed by washout with initial pH 5.8 medium.



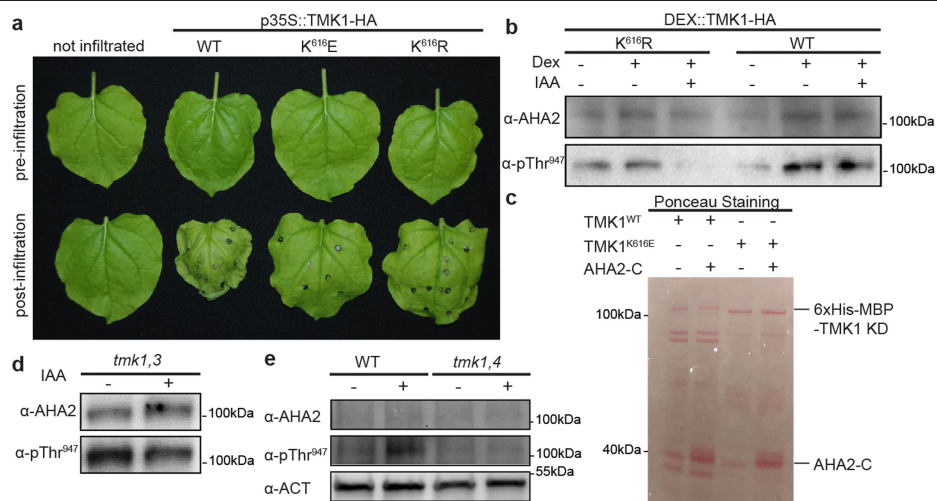
Extended Data Fig. 3 | H^+ -ATPase activation counteracts auxin-mediated apoplast alkalization and growth inhibition. **a, b,** Apoplastic pH of WT elongating root cells pre-treated (yellow) with $1\mu M$ cycloheximide (CHX) for 3min (**a**), or $50\mu M$ cordycepin (CORD) for 32min (**b**) followed by addition of $5nM$ IAA (pink). Mean of 3 (**a**) or 4 (**b**) roots+s.d. **c,** $10nM$ IAA induced Thr⁹⁴⁷ phosphorylation in roots using AHA2 and pThr⁹⁴⁷ specific antibodies. Band intensities of the different lanes were quantified by the Gel Analysis function in ImageJ. **d,** Measurement of *DR5::LUC* luminescence intensity in the root tip after $10\mu M$ FC, $10nM$ IAA and IAA+FC co-treatment. $n>3$ roots. IAA and IAA+FC are significantly different from the mock ($P\leq 0.0001$). No significant difference between IAA and IAA+FC (ns, $P>0.05$). Two-way ANOVA. **e–k,** FC and IAA counteract each other. In vRootchip, addition of IAA still increased apoplastic pH (**e**) and inhibited root growth (**f**) in presence of FC, while addition of FC decreased apoplastic pH (**j**) and promoted root growth (**k**) in presence of IAA. Upon simultaneous addition of $10\mu M$ FC and $10nM$ IAA, both apoplastic pH (Fig 2d) and root growth (**g**) were less affected than by IAA alone. Shaded area represents the duration of the treatments. Mean of 4 roots+s.d. **** $P\leq 0.0001$

between IAA and IAA+FC from 0–31min (**g**), Two-way ANOVA. **(h–i)** Steady-state 1h root growth after FC, IAA and co-treatment was obtained by scanner. $1\mu M$ FC and $10nM$ IAA were used in (**h**) while $10\mu M$ FC and $2nM$ IAA were used in (**i**). $n>9$ roots. Box plot depicts minimum to maximum, mean±s.d. ns $P>0.05$, * $P\leq 0.05$, ** $P\leq 0.01$, **** $P\leq 0.0001$, One-way ANOVA (**h, i**). **l,** Dose-response of auxin-induced root growth inhibition of *aha* single mutants. $n>22$ roots. Relative GR is ratio between auxin-affected growth and mock for the same genotype. ns $P>0.05$, ** $P\leq 0.01$, *** $P\leq 0.001$, Welch ANOVA. **m,** Quantitative Real-time PCR on the *AHA1, 2, 7, 11* expression in root tips of *AtTAS1c-AHA#2* and #4. The expression level was normalized to *EF1a* as housekeeping gene. Mean of 6 biological replicates in 3 technical replicates+s.d. Box plot depicts minimum to maximum, mean±s.d. ns $P>0.05$, * $P\leq 0.05$, ** $P\leq 0.01$, *** $P\leq 0.001$, One-way ANOVA. **n,** Dose-response of auxin-induced root growth inhibition of *AtTAS1c-AHA* lines and *ost2-3D* mutants reveals hypersensitivity and resistance respectively to IAA in comparison to WT ($n>15$ roots). Relative GR is calculated as mentioned in (**l**). ns $P>0.05$, * $P\leq 0.05$, ** $P\leq 0.01$, *** $P\leq 0.001$, **** $P\leq 0.0001$, Welch ANOVA.



Extended Data Fig. 4 | TMK1 interacts with PMH⁺-ATPase. **a**, TMK1 expression pattern in the elongation zone (EZ), meristematic and transition zone (MZ-TZ) in the primary root shown by pTMK1::TMK1-GFP. Scale bar=60 μm. **b, c**, IP-MS/MS on pTIR1::TIR1-VENUS in *tir1-1* (**b**) and pAFB1::AFB1-VENUS in *afb1-3* (**c**) under mock condition compared to 1h 50μM MG132 pre-treatment and 2min 100nM IAA treatment. Proteins surpassing the threshold FDR of 0.05 are marked. Green depicts the respective bait protein and red depicts known members of the SCF E3 ubiquitin ligase complex. Pulldowns were performed in triplicate, LFQ analysis. **d**, IP-MS/MS on pTMK1::TMK1-GFP. Peptides corresponding to AHA1/2 are shown in red. p-values are calculated based on

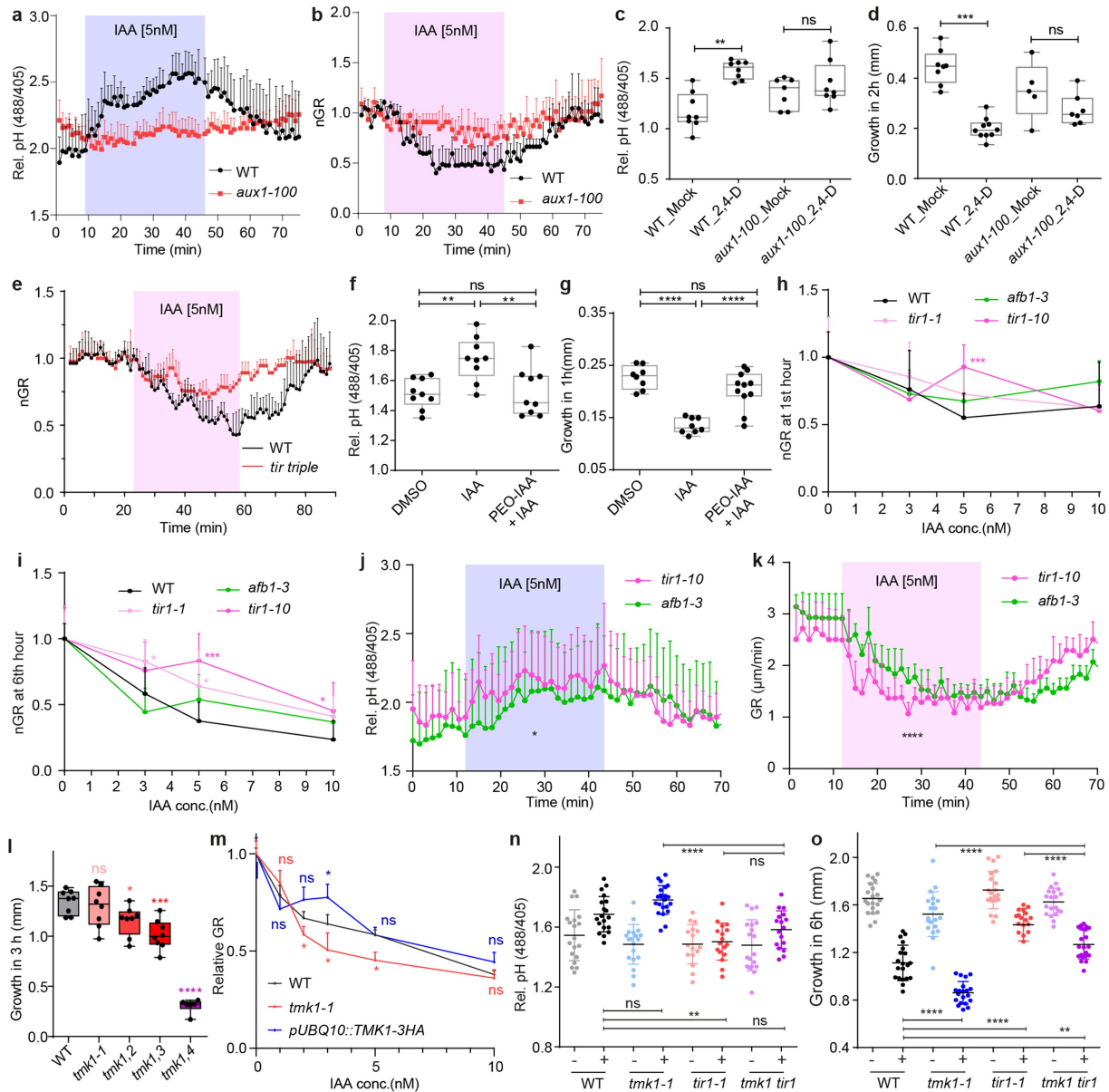
three biological replicates using two-sided t-tests. **e**, Co-IP of pAHA2::AHA2-GFP roots, followed by Western blot detection of TMK1 and Thr⁹⁴⁷-phosphorylated AHA2 after 100nM IAA for 30min. Auxin did not affect interaction, but induced AHA2-phosphorylation. Input of pAHA2::AHA2-GFP roots was the control. **f**, Bimolecular Fluorescent Complementation (BiFC) in *Nicotiana benthamiana* leaves transiently transformed with the reciprocal controls for Fig. 3b: YFP^N-TMK1, AHA2-YFP^C or both. Scale bar=10μm. **g**, Demonstration of specific interaction between YFP^N-TMK1^{K616R} and AHA2-YFP^C as no complementation was observed in the leaves expressing YFP^N-TMK1^{K616R} and AUX1-YFP^C or leaves expressing YFP^N-AHA2 and AUX1-YFP^C. Scale bar=100μm.



Extended Data Fig. 5 | TMK1 directly phosphorylates PM H⁺-ATPases.

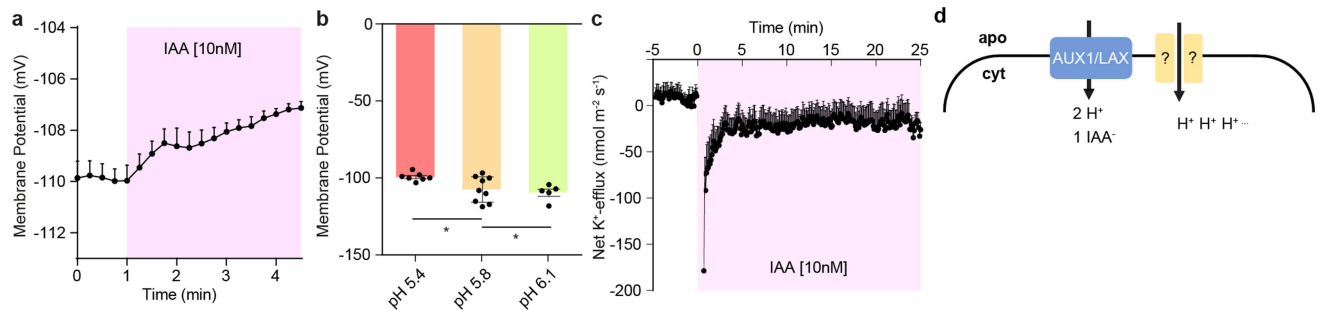
a, Wilting *N. benthamiana* leaves that transiently express *TMK1*^{WT} and ATP-site mutated forms *TMK1*^{K616E} or *TMK1*^{K616R}. **b**, Western blot analysis of the AHA2 levels and the Thr947 phosphorylation in roots of *DEX::TMK1*^{WT} or *TMK1*^{K616R}-HA treated +/- DEX (30μM for 24h) and +/- IAA (100nM for 1h). **c**, Ponceau-stained SDS-PAGE gel as

loading control for *in vitro* kinase assay with [γ-³²P]-ATP, substrate C-terminal AHA2 (AHA2-C) and the intracellular kinase domain of *TMK1*^{WT} or kinase dead *TMK1*^{K616E}. **d**, **e**, Western blot detection of AHA2 levels and Thr947 phosphorylation in *tmk1,3* roots (**d**) or *tmk1,4* roots (**e**) treated with 100nM IAA for 1h. WT control for (**d**) is shown in Fig. 3e.



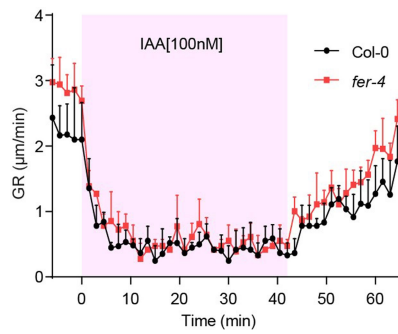
Extended Data Fig. 6 | Cytosolic TIR1/AFB mediates rapid apoplast alkalization and root growth inhibition. a, b, Apoplastic alkalization (a) and root growth inhibition (b) in response to IAA measured in *aux1-100* mutant compared to WT roots in vRootchip. Mean of 3 roots+s.d. **** $P \leq 0.0001$, Two-way ANOVA. **c, d,** Apoplastic alkalization (c) and root growth inhibition (d) in response to 2,4-D in *aux1-100* mutant compared to WT roots. Steady state pH measured 30min after 100nM 2,4-D treatment. Mean of >6 roots+s.d., One-way ANOVA (c). (d) Growth obtained in 2h was captured by scanner. Mean of >4 roots+s.d., One-way ANOVA. ns $P > 0.05$, ** $P \leq 0.01$, *** $P \leq 0.001$. **e,** Root growth of *tir triple* mutants compared to WT in response to 5nM IAA in the vRootchip. Mean of 3, 2 roots+s.d. **** $P \leq 0.0001$, two-way ANOVA. **f, g,** Apoplastic pH (f) and root growth (g) after 10 μM PEO-IAA and 5nM IAA. The steady state pH was measured 30min after treatments, while the root growth obtained in 1h was recorded by scanning. Mean of >7 roots+s.d., ns $P > 0.05$, ** $P \leq 0.01$, **** $P \leq 0.0001$, One-way ANOVA. **h, i,** Dose-response of auxin-induced root growth inhibition of *tir1-1*, *tir1-10* and *afb1-3* mutants reveals

slight resistance to 5nM IAA in comparison to WT ($n > 6$ roots). Relative GR is calculated as the ratio of GR at 1h (h) or 6h (i) after IAA treatments relative to mock-treated GR of the same genotype. Mean+s.d. * $P \leq 0.05$, *** $P \leq 0.001$, One-way ANOVA. **j, k,** Apoplastic pH (j) and root growth (k) analysis comparing *tir1-10* null mutant and *afb1-3* mutants in response to IAA in vRootchip. Shaded area represents the duration of the treatment. Mean of 4 roots for each treatment+s.d. $P \leq 0.0001$ (j) and $P \leq 0.05$ (k), Two-way ANOVA. **l,** Steady-state root growth over 6h in *tmk1*-related mutants. $n = 6$ roots for *tmk1-4*; $n > 26$ for others. Mean+s.d. Box plot depicts minimum to maximum, mean+s.d. **** $P \leq 0.0001$, One-way ANOVA. **m,** Dose-response of auxin-induced root growth inhibition of *pUBQ10::TMK1-3HA* compared to WT and *tmk1-1*. Relative GR is the ratio between auxin-affected growth to the mock growth in the same genotype. Mean of >7 roots+s.d., ns $P > 0.05$, * $P \leq 0.05$, Welch ANOVA. **n, o,** Raw data for Fig. 4d, e, respectively. $n > 16$ roots. Box plot depicts minimum to maximum, mean+s.d. ns $P > 0.05$, ** $P \leq 0.01$, **** $P \leq 0.0001$, One-way ANOVA.

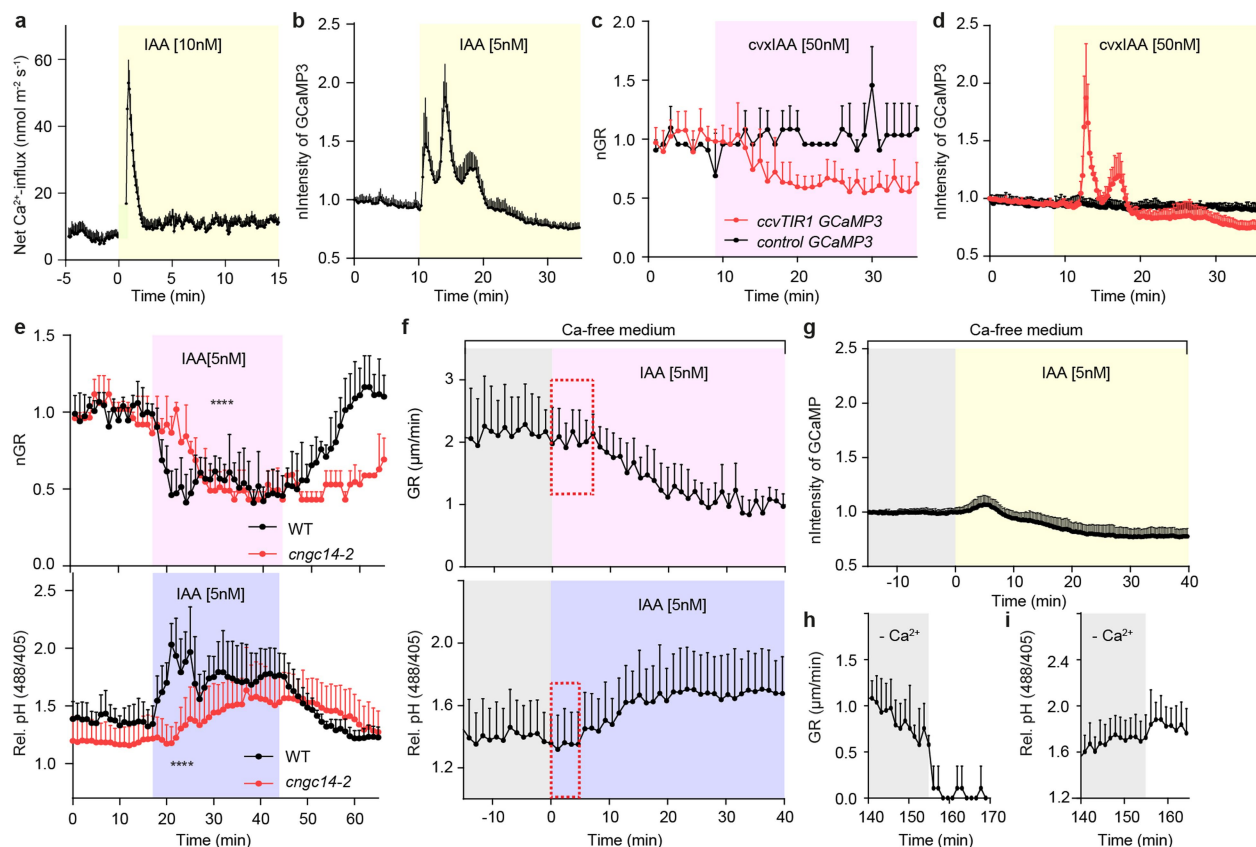


Extended Data Fig. 7 | PM potential and AUX1 involvement in auxin-induced apoplast alkalinization. Since auxin causes simultaneously membrane depolarization²⁵ and apoplast alkalinization, both of which are interdependent and required for growth, we addressed which of them mediates the auxin effect on root inhibition. By manipulating the external pH, we found that pH and growth were correlated (Fig. 1d–g) while membrane potential (MP) was uncoupled (**a, b**). Additionally, we observed that K⁺ efflux (**c**) compensates auxin-induced H⁺ and Ca²⁺ influx (Extended Data Fig. 2c, Extended Data Fig. 8a), suggesting that auxin-induced MP change is the result of complex ion fluxes, while H⁺ influx and resulting apoplastic pH change for growth regulation is just a subset of those. **a, b**, Membrane potential recorded by invasive micro-electrode in root elongating cells with IAA treatment (magenta). 4 roots+s.e.m. (**a**). Membrane potential measured in root elongating cells after 40min incubation in different pH medium. n>5 roots±s.e.m. *P≤0.05, One-way ANOVA (**b**). Alkaline medium, which alkalinized the apoplast and inhibited root growth (Fig. 1d, e) mimicking the auxin effect, did not result in membrane depolarization. Acidic medium, which acidified the apoplast and promoted root growth (Fig. 1f, g) depolarized membrane. MP is thus uncoupled from growth and apoplastic pH. **c**, PM net K⁺ efflux measured by a non-invasive microelectrode before and after 10nM IAA treatment in the elongating zone of

WT roots. 16 roots+s.e.m. **d**, Scheme showing AUX1/LAX-mediated IAA/2H⁺ symport and mechanistically elusive H⁺ influx. IAA/2H⁺ symport by AUX1 auxin influx carrier was proposed¹⁷ a possible mechanism of auxin-induced H⁺ influx and apoplast alkalinization. Comparison of H⁺ influx rates in root hair cells¹⁷, or elongating root epidermal cells (Extended Data Fig. 2c) and conservative estimates of AUX1-mediated ³H-IAA transport in *Xenopus* oocytes^{24,64} argue against this. Below we show that calculations based on data of *Xenopus* oocytes, primary root and root hairs suggest that AUX1-mediated H⁺ symport is not sufficient to account for the auxin-induced H⁺ fluxes: (1) ³H-IAA transport in the AUX1 overexpressing *Xenopus* oocytes after 100nM ³H-IAA²⁴ is ca. 2.6x10⁻¹⁴ mol min⁻¹. The min. diameter of the *Xenopus* oocyte at stage V/VI⁶⁴ is ca. 1.0mm, so the surface area is minimally 3.142x10⁻⁶ m². The max. speed of IAA uptake across the membrane is calculated as: 2.6 x 10⁻¹⁴ mol/(60s x 3.142x10⁻⁶ m²) = 1.38x10⁻¹⁰ mol m⁻² s⁻¹. Based on 2H⁺ per IAA¹⁷, the max. speed of AUX1-symported H⁺ is 2.76x10⁻¹⁰ mol m⁻² s⁻¹. (2) H⁺ uptake after 10nM IAA (ten times less than in *Xenopus*) in *Arabidopsis* root elongating cells: 1.7x10⁻⁸ mol m⁻² s⁻¹ (Extended Data Fig. 2c). This is still 62 times more than the conservatively estimated max. speed in (1). (3) H⁺ uptake NAA in *Arabidopsis* root hairs¹⁷ is ca. 1.0x10⁻⁷ mol m⁻² s⁻¹. This is 362 times more than the conservatively estimated max. speed in (1).



Extended Data Fig. 8 | *FER* does not mediate auxin-induced rapid growth inhibition. Root growth of *fer-4* compared to Col-0 in response to application and washout of 100nM IAA in vRootchip. Shaded area indicates IAA treatment. Mean of 5 roots for Col-0 and 3 for *fer-4* + s.d. ns, $P > 0.05$, Two-way ANOVA.



Extended Data Fig. 9 | TIR1-mediated Ca^{2+} signalling contributes to auxin-induced apoplast alkalization. Another rapid output of TIR1/AFB perception mechanism are cytosolic Ca^{2+} transients in root hairs¹⁷. Therefore, we evaluated Ca^{2+} transients in apoplast alkalization and root growth inhibition. Using vRootchip, GCaMP3 Ca^{2+} marker³³, non-invasive microelectrodes and cvxIAA-ccvTIR1 system²⁸, we confirmed that auxin via TIR1/AFB triggered rapid Ca^{2+} influx correlates with root growth inhibition (a-d). We noted a distinct Ca^{2+} response measured by the microelectrode (a-b) and GCaMP3 (c). Namely, Ca^{2+} channels are activated at the plasma membrane resulting in net influx, while the GCaMP3 reported more complex responses possibly involving intracellular Ca^{2+} storage and release. Moreover, the use of cvxIAA-ccvTIR1 (d) provided additional proof that TIR1-mediated auxin perception activates Ca^{2+} signalling. Further, we verified that mutants in the Ca^{2+} permeable cation channel *Cyclic NUCLEOTIDE-GATED CHANNEL 14* (*CNGC14*) have delayed auxin-induced apoplast alkalization and root growth inhibition (e) similarly as reported¹⁴. Furthermore, depletion of external Ca^{2+} resulted in attenuated auxin-induced Ca^{2+} spike, delayed apoplast alkalization and growth inhibition (b, f, g). Ca^{2+} addition resulted in rapid growth inhibition (h, i). These observations collectively suggest that TIR1/AFB-mediated Ca^{2+} signalling is part of the mechanism for auxin-induced rapid apoplast alkalization and growth inhibition. a, PM net Ca^{2+} influx measured

by a non-invasive microelectrode before and after 10nM IAA treatment in the elongating zone of WT roots. 9 roots+s.e.m. b, Normalized fluorescence intensity of GCaMP3 , cytosolic Ca^{2+} marker, in elongating cells responding to 5nM IAA treatment in vRootchip. The intensity was normalized to the initial intensity of the same root. Mean of 7 roots+s.d. Note the three peaks in cytosol compared to the single major peak outside of cells (a). c, d, Root growth (c) and fluorescence intensity in elongating cells (d) in GCaMP3 crossed into *ccvTIR1* compared to control. Growth rate and intensity are normalized to the pre-stimulus value. Mean of 7 for *ccvTIR1* and 2 for control+s.d. **** $P \leq 0.0001$, Two-way ANOVA. e, Root growth (upper graph) and apoplastic pH (lower graph) analysis in *cngc14-2* and WT in response to IAA in vRootchip. Mean of 5 roots for WT and 3 for *cngc14-2*+s.d. **** $P \leq 0.0001$, Two-way ANOVA. f, g, Root growth (upper graph in f) and apoplastic pH (lower graph in f) in WT, as well as cytosolic Ca^{2+} analysis in GCaMP3 reporter marker line in vRootchip (g) with 140min pre-treatment of Ca^{2+} free medium (grey) followed by 5nM IAA addition (magenta for growth, blue for pH in f and yellow for Ca^{2+} in g). Auxin induced significant less Ca^{2+} response in Ca^{2+} free medium, compared to normal medium in (b). The red dotted square marked the non-responsive delay after auxin. Mean of 5 (f) and 6 (g) roots+s.d. h, i, Root growth (h) and apoplastic pH (i) analysis in WT upon Ca^{2+} addition after 140min Ca^{2+} free medium in the presence of 5nM IAA in vRootchip. Mean of 5 roots+s.d.

Reporting Summary

Nature Portfolio wishes to improve the reproducibility of the work that we publish. This form provides structure for consistency and transparency in reporting. For further information on Nature Portfolio policies, see our [Editorial Policies](#) and the [Editorial Policy Checklist](#).

Statistics

For all statistical analyses, confirm that the following items are present in the figure legend, table legend, main text, or Methods section.

n/a Confirmed

- ☐ ☒ The exact sample size (n) for each experimental group/condition, given as a discrete number and unit of measurement
- ☐ ☒ A statement on whether measurements were taken from distinct samples or whether the same sample was measured repeatedly
- ☐ ☒ The statistical test(s) used AND whether they are one- or two-sided
Only common tests should be described solely by name; describe more complex techniques in the Methods section.
- ☒ ☐ A description of all covariates tested
- ☒ ☐ A description of any assumptions or corrections, such as tests of normality and adjustment for multiple comparisons
- ☐ ☒ A full description of the statistical parameters including central tendency (e.g. means) or other basic estimates (e.g. regression coefficient) AND variation (e.g. standard deviation) or associated estimates of uncertainty (e.g. confidence intervals)
- ☐ ☒ For null hypothesis testing, the test statistic (e.g. F , t , r) with confidence intervals, effect sizes, degrees of freedom and P value noted
Give P values as exact values whenever suitable.
- ☒ ☐ For Bayesian analysis, information on the choice of priors and Markov chain Monte Carlo settings
- ☒ ☐ For hierarchical and complex designs, identification of the appropriate level for tests and full reporting of outcomes
- ☒ ☐ Estimates of effect sizes (e.g. Cohen's d , Pearson's r), indicating how they were calculated

Our web collection on [statistics for biologists](#) contains articles on many of the points above.

Software and code

Policy information about [availability of computer code](#)

Data collection	<p>The microscope images were collected using Zen 2011 (blue edition).</p> <p>The medium flow in the vRootchip were controlled by the Arduino and Processing software with scripts described in the Extended Data Scripts in the manuscript.</p> <p>The scanning pictures were captured automatically by using Autolt with the code described in DOI: 10.21769/BioProtoc.2685.</p>
Data analysis	<p>The pH analysis on the microscope image using the HPTS dye or PM-cyt reporter line applied the script described in doi.org/10.1073/pnas.1613499114.</p> <p>The cortical microtubule orientation analysis was done with script Fibril Tool described in doi.org/10.1038/nprot.2014.024, and the script Bioline described in doi.org/10.3390/ijms20133337.</p> <p>The root growth imaged in the vRootchip was analysed as described in doi: 10.1038/s41477-018-0190-1.</p> <p>The root growth captured by scanner over time was analysed with the script Root Growth Tracker described in doi.org/10.15479/AT:ISTA:8294.</p> <p>All the time-series images are stabilized in FIJI (https://imagej.net/Fiji) by the StackReg Fiji plugin in the 'translation' or 'rigid body' option.</p> <p>All statistical analysis were done in GraphPad Prism 6 or 8.</p>

For manuscripts utilizing custom algorithms or software that are central to the research but not yet described in published literature, software must be made available to editors and reviewers. We strongly encourage code deposition in a community repository (e.g. GitHub). See the Nature Portfolio [guidelines for submitting code & software](#) for further information.

Data

Policy information about [availability of data](#)

All manuscripts must include a [data availability statement](#). This statement should provide the following information, where applicable:

- Accession codes, unique identifiers, or web links for publicly available datasets
- A description of any restrictions on data availability
- For clinical datasets or third party data, please ensure that the statement adheres to our [policy](#)

Data availability statement

The data and full blots that support the findings presented here are available within the paper and its Supplementary Information. All source data used for graphs are available. Full blots are in SI.

Field-specific reporting

Please select the one below that is the best fit for your research. If you are not sure, read the appropriate sections before making your selection.

☒ Life sciences ☐ Behavioural & social sciences ☐ Ecological, evolutionary & environmental sciences

For a reference copy of the document with all sections, see nature.com/documents/nr-reporting-summary-flat.pdf

Life sciences study design

All studies must disclose on these points even when the disclosure is negative.

Sample size	All experiments were analyzed with multiple technical/biological replicates. Note for one single vRootchip experiments, the sample size is max. 8 roots due to the practical reasons: only 8 roots can be inserted into the device, and 4 roots when there were two genotypes; besides, 1 min interval of imaging both pH and growth on the same root limits the number of samples. Details can be found in DOI: 10.1038/s41477-018-0190-1. Therefore, we perform multiple replicates of the experiment.
Data exclusions	No data were excluded from the analysis.
Replication	All attempts at replication were successful.
Randomization	Samples were always randomly allocated into experimental groups for analysis.
Blinding	The analysis was performed blind wherever possible. For the scanner growth assays, we did double blind analysis.

Reporting for specific materials, systems and methods

We require information from authors about some types of materials, experimental systems and methods used in many studies. Here, indicate whether each material, system or method listed is relevant to your study. If you are not sure if a list item applies to your research, read the appropriate section before selecting a response.

Materials & experimental systems

n/a	Involved in the study
<input type="checkbox"/>	<input checked="" type="checkbox"/> Antibodies
<input checked="" type="checkbox"/>	<input type="checkbox"/> Eukaryotic cell lines
<input checked="" type="checkbox"/>	<input type="checkbox"/> Palaeontology and archaeology
<input checked="" type="checkbox"/>	<input type="checkbox"/> Animals and other organisms
<input checked="" type="checkbox"/>	<input type="checkbox"/> Human research participants
<input checked="" type="checkbox"/>	<input type="checkbox"/> Clinical data
<input checked="" type="checkbox"/>	<input type="checkbox"/> Dual use research of concern

Methods

n/a	Involved in the study
<input checked="" type="checkbox"/>	<input type="checkbox"/> ChIP-seq
<input checked="" type="checkbox"/>	<input type="checkbox"/> Flow cytometry
<input checked="" type="checkbox"/>	<input type="checkbox"/> MRI-based neuroimaging

Antibodies

Antibodies used

All the descriptions are included in the Methods.

The anti-AHA2 and anti-Thr947 AHA2 antibody were shared by Toshinori Kinoshita and used as described previously at final dilution of 1:5000 in TBST buffer + 3% BSA, followed by anti-rabbit IgG secondary antibody conjugated to horseradish peroxidase (HRP) (GE Healthcare, NA934) at a dilution of 1:10000 and chemiluminescence reaction (SuperSignal West Femto, Thermo Scientific). To allow multiple antibody detections using the same PVDF membrane, mild stripping was performed using 15 g/L glycine, 1 g/L SDS, 10 mL/L Tween-20 buffer at pH 2.2 for 2-5 minutes.

Anti-HA-HRP (Sigma-Aldrich, clone BMG 3F10 monoclonal antibody - Cat no: 12013819001), anti-FLAG -HRP (Sigma-Aldrich, clone M2

Validation

- Cat no:A8592) and anti-GFP JL8 antibodies (Living Colors monoclonal antibody, Clontech - Cat no: 632381) were commercially obtained.

Anti-AHA2 and anti-Thr947 AHA2 antibody were validated both for species and protein specificity by Toshinori Kinoshita and colleagues (Hayashi, Y. et al. Biochemical characterization of in vitro phosphorylation and dephosphorylation of the plasma membrane H⁺-ATPase. Plant Cell Physiol. 51, 1186-1196 (2010)). anti-HA-HRP, anti-FLAG-HRP and anti-GFP antibodies are commercially available (indicated above) and were validated by the producers.